A material length scale based methodology to assess static strength of notched additively manufactured polylactide (PLA)

Adnan A. Ahmed, Luca Susmel

Department of Civil and Structural Engineering, the University of Sheffield,
Mappin Street, Sheffield S1 3JD, UK

ABSTRACT

The Theory of Critical Distances (TCD) is the name which has been given to a group of design methodologies that all make use of a material length scale parameter to post-process the local linear-elastic stress fields in the vicinity of the crack initiation locations. The aim of the present investigation is to check whether the simple linear-elastic TCD is successful in predicting static strength of notched components made of 3D-printed polylactide (PLA), with PLA being a thermoplastic aliphatic polyester that is produced from renewable biodegradable resources. The accuracy and reliability of the TCD in estimating the static strength of additively manufactured (AM) PLA was assessed against a large number of experimental results generated by testing, under tensile loading as well as under bending, AM notched specimens containing different geometrical features (open notches included). The TCD was seen to be highly accurate, its systematic use resulting in estimates falling mainly within an error interval of about 20%. This result is certainly very relevant since it demonstrates that the linear-elastic TCD can be used successfully to design against static loading notched components of AM PLA by directly post-processing the results from simple linear-elastic Finite Element (FE) models.

Keywords: additive manufacturing, polylactide (PLA), Theory of Critical Distances, material length scale

Nomenclature

a, B, W	dimensions of the C(T) specimens according to ASTM D5045–14
E	Young's modulus
F_f	failure force
K_c	fracture toughness
K_{Ic}	plane strain fracture toughness
L	critical distance
Oθr	polar coordinates
Oxy	local system of coordinates
Ox_py_p	3D-printer principal system of coordinates
r_n	notch root radius
S_D	standard deviation
t	specimen's thickness
t_s	shell thickness
w_n, w_g	net and gross width
θ_p	manufacturing angle
σ_o	inherent strength
$\sigma_{0.2\%}$	0.2% proof stress
σ_1	maximum principal stress
σ_{eff}	effective stress
σ_f	failure nominal stress referred to the net area
σ_{nom}	nominal stress
σ_{UTS}	ultimate tensile strength
σ_x, σ_y, τ_{xy}	local stress components
α	notch opening angle

1. Introduction

Whether as a replacement for existing production methods on economic grounds, or because of the ability to produce components that have up until now been impossible, it is clear that additive manufacturing (AM) will certainly have an impact on the future of the manufacturing arena.

The growth in the AM industry is predicted by many to be rapid and substantial, as more companies develop production equipment, more materials become available and more end-user industries adopt the technology. The global value of the industry is currently estimated to reach over $10 billion by 2021.

The ability to produce customised products for the individual has already been demonstrated in a number of sectors (such as, for instance, automotive, aerospace, civil infrastructure and medical applications), but this flexibility could offer huge potential in the consumer goods market. Production lines implementing manufacturing on demand could also be created using layer based technologies.

AM offers new possibilities also in the choice of materials. Thanks to the systematic R&D work that has been done worldwide since the end of the last century, nowadays it is possible to additively manufacture metals, polymers, composite materials and concrete.

Examination of the state of the art demonstrates that, over the last two decades, the scientific community has focussed its attention mainly on the technological aspects. In more detail, the core aim of these investigations was primarily developing and optimising AM techniques that allow both the overall quality of the fabricated objects and the productivity level to be increased, with this being accompanied by a reduction of the associated manufacturing costs. In contrast, little research work has been carried out so far in order to investigate the structural/cracking behaviour of AM materials subjected to static, dynamic and time-dependent loading, with this limiting a proper exploitation of this powerful fabrication technology. In this context, one of the key features of AM is that it can be used to manufacture objects characterised by intricate shapes which would represent a challenge to traditional "subtractive" fabrication processes. From a structural integrity view point, since the form of AM components can be extremely complex, the presence of geometrical features leads to localised stress/strain concentration phenomena that reduce markedly the overall strength of the components themselves. Therefore, to allow AM to be used systematically in situations of practical interest, structural engineers need to be provided with accurate and simple design methodologies specifically developed to assess 3D-printed materials weakened by geometrical features of all kinds. With regard to these bespoke design techniques, it is important to point out that, owing to AM's *modus operandi*, they should be formalised so that the structural assessment can be performed by directly post-processing the results from conventional FE analyses, with the same three-dimensional virtual models being used to inform also the subsequent manufacturing process.

As far as static assessment of notched components is concerned, much experimental evidence suggests that the so-called Theory of Critical Distances (TCD) [1] is certainly the most powerful candidate to be used in situations of practical interest to design AM notched components against static loading. The key advantage of the TCD is that its usage does not require complex non-linear constitutive models [2-4], with this holding true independently of the level of ductility characterising the material being assessed [5, 6]. Further, since the TCD takes directly into account the morphology of the assessed material via suitable length scale parameters [1], it is capable of accurate estimates regardless shape and sharpness of the geometrical features

being designed [5, 7]. Lastly, by its nature, the TCD can be applied by making direct use of linear-elastic stress fields determined numerically via commercial FE software packages [8].

Polylactide - $(C_3H_4O_2)_n$ - is a linear thermoplastic aliphatic polyester that is made through industrial fermentation of plant materials such as, for instance, sugarcane, potatoes, tapioca roots, chips and corn starch. Polylactide (PLA) is a biodegradable, absorbable and biocompatible material and is widely employed in different industrial sectors to manufacture components having complex shape. Particularly relevant is the use of PLA to manufacture medical devices designed to biodegrade within 6-12 months. Together with acrylonitrile butadiene styrene (ABS), PLA is also one of the most common polymers that is used to additively manufacture objects by employing low-cost commercial 3D-printers.

The mechanical/cracking behaviour of AM PLA as well as its strength are affected by a number of important technological variables that include: layer thickness, infill percentage, nozzle size, manufacturing orientation, filling pattern, filling rate, feed rate, manufacturing rate, and filling temperature [9-13]. In more detail, the ultimate tensile strength (UTS, σ_{UTS}) of AM PLA is seen to decrease not only as the infill angle increases [10, 13], but also as the shell thickness decreases [10]. Further, given the manufacturing direction and the width of the superficial shell, the UTS is influenced markedly also by the thickness of the layers [10, 11]. In the same way as σ_{UTS}, also the elastic modulus, E, of AM PLA is seen to decrease as the infill angle increases, with the relationship between σ_{UTS} and E being almost linear [10]. In general terms, compared to conventionally manufactured PLA, the 3D-printing process produces a material that is characterised by a higher level of crystallinity and a lower level of ductility, with these being accompanied by an increase of the fracture toughness as well as of the strain rate sensitivity [12]. The elastic part of the total deformation of AM PLA is seen to be characterised by a limited level of anisotropy, whilst its plastic response is mainly ductile and orthotropic [12, 13]. In this context, much experimental evidence suggests that the overall mechanical behaviour of PLA is predominantly brittle, with the level of ductility changing as the manufacturing direction varies [12]. Finally, it is worth pointing out that the mechanical properties of AM PLA are also affected by the pigments that are used to colour the parent material [14].

In this complex and challenging scenario, the present paper aims to investigate the accuracy of the linear-elastic TCD in estimating the static strength of notched components of AM PLA.

2. Fundamentals of the Theory of Critical Distances

The key feature of the TCD [1] is that static strength of notched/cracked components is assessed by making use of a characteristic length which is directly related to the microstructural features of the material being designed. From a practical point of view, this

theory estimates the extent of damage by post-processing the entire linear-elastic stress fields acting on a pre-defined material region in the vicinity of the assumed crack initiation locations. Taking as a starting point this general theoretical framework, the TCD can be formalised in different ways by simply changing the geometrical characteristics of the physical domain that is used to calculate the required effective stress, σ_{eff} [1, 15]. In particular, the so-called Volume Method, which represents the most complex way to implement the TCD, calculates σ_{eff} by averaging the stress over a hemisphere centred at the tip of the notch/crack being assessed [15]. The above method can be simplified by using a bi-dimensional integration domain instead. In more detail, as postulated by the so-called Area Method, σ_{eff} can also be determined by averaging the stress over a semi-circular area centred at the apex of the assessed stress concentrator [1, 16]. The Area Method can be formalised mathematically by referring to the notched component sketched in Figure 1a. Initially, the hypothesis is formed that the material characteristic length, L, needed to apply the TCD is known from the experiments, with the problem of its determination being discussed later in the present section. By post-processing the local-linear elastic stress field in the vicinity of the notch/crack under investigation, the effective stress can be calculated according to the Area Method as follows [1, 16] (Fig. 1b):

$$\sigma_{eff} = \frac{4}{\pi L^2} \int_0^{\pi/2} \int_0^{L} \sigma_1(\theta, r) \cdot r \cdot dr \cdot d\theta \tag{1}$$

where σ_1 is the maximum principal stress, whereas $O\theta r$ is a local system of polar coordinates that is centred at the tip of the assessed stress raiser (see Fig. 1a).

According to the way the Volume Method and the Area Method calculate σ_{eff}, it is possible to argue that the TCD assesses the static strength of engineering materials weakened by stress concentration phenomena by directly manipulating the local linear-elastic stress field acting on a specific material process zone [1, 17, 18]. Accordingly, in the TCD framework, this process zone can be thought of as that portion of material which controls the overall static strength of the notched component being designed. In this setting, the size of the representative volume as defined above is seen to depend on the dominant source of microstructural heterogeneity, on the micro-mechanical material properties as well as on the characteristics of the physical processes governing the local cracking behaviour [17, 18]. By combining the *modus operandi* of the Volume/Area Method (Fig. 1b) with this fairly articulated reasoning, it is logical to come to the conclusion that the size of the process zone has to be of the order of the material characteristic length, L.

Certainly, both the Volume Method and the Area Method represent very elegant formalisations of the TCD. However, using these two approaches in situations of practical

interest is quite cumbersome, since bespoke numerical/analytical tools have to be employed so that in the presence of complex geometries the local linear-elastic stress can be averaged accurately over the relevant integration domains.

Fortunately, the usage of the TCD can be greatly simplified by observing that this theory can also be applied in the form of either the Line Method or the Point Method [1, 16, 19]. In more detail, the Line Method postulates that the effective stress can be determined by averaging the stress along a linear path having length equal to 2L, i.e. [1] (Fig. 1c):

$$\sigma_{eff} = \frac{1}{2L}\int_{0}^{2L} \sigma_y(\theta = 0, r)\cdot dr \tag{2}$$

where, according to Fig. 1c, σ_y is the stress perpendicular to the notch/crack bisector. The Point Method instead assumes that σ_{eff} is simply equal to the linear-elastic stress determined at a distance from the notch/crack apex equal to L/2, i.e. [1] (Fig. 1d):

$$\sigma_{eff} = \sigma_y\left(\theta = 0, r = \frac{L}{2}\right) \tag{3}$$

After determining the effective stress according to either the Volume, Area, Line, or Point Method, the subsequent problem to be addressed is the determination of an appropriate reference strength - i.e., the so-called inherent material strength, σ_o [1]. σ_o is seen to depend primarily on the mechanical response of the material being designed. In particular, when the mechanical behaviour of the material under investigation is predominantly brittle (for instance, fibre reinforced composites [19] and engineering ceramics [20]), σ_o is seen to be invariably equal to the UTS. In contrast, when materials deform plastically before final breakage takes place (for instance, metals [1, 3-5] and quasi-brittle polymers [6, 21]), σ_o becomes larger than σ_{UTS}. These considerations should make it evident that the only way to determine inherent strength σ_o accurately is by running appropriate experiments [22, 23].

Having quantified both σ_{eff} and σ_o, the notched/cracked material being assessed is then supposed not to fail as long as the effective stress calculated according to either the Volume, Area, Line, or Point Method is lower than the inherent material strength, i.e.:

$$\sigma_{eff} < \sigma_o \tag{4}$$

The reasoning summarised above makes it evident that the TCD based design procedure reviewed in the present section can be used in situations of practical interest as long as both critical distance L and inherent strength σ_0 are known for the specific material being designed. These two material properties can be determined experimentally by using the results generated by testing specimens containing notches of different sharpness. In more detail, as shown in Fig. 1e, consider the two stress-distance curves plotted, in the incipient failure condition, by post-processing the results from two sets of tests involving a sharp and blunt notch, respectively [1, 3, 8]. In accordance with the PM's *modus operandi*, the coordinates of the point at which these two curves intersect each other allow L and σ_0 to be determined unambiguously (Fig. 1e).

To conclude, it is worth observing that the experimental strategy summarised in Fig. 1e can be used to estimate L and σ_0 not only for ductile, but also for brittle materials. However, as far as brittle materials are concerned, since $\sigma_0=\sigma_{UTS}$ [1], the material characteristic length can also be determined directly via the following well-known relationship [1, 19]:

$$L = \frac{1}{\pi}\left(\frac{K_{Ic}}{\sigma_{UTS}}\right)^2 \tag{5}$$

where K_{Ic} is the plane strain fracture toughness determined according to Linear Elastic Fracture Mechanics (LEFM).

3. Fabrication of the specimens and static testing

In order to check whether the linear-elastic TCD is successful also in estimating static strength of notched 3D-printed PLA, a large number of specimens containing different geometrical features were manufactured by employing as parent material white filaments of New Verbatim PLA with diameter equal to 2.85mm. The specimens shown in Figs 2 and 3 were fabricated by employing 3D-printer Ultimaker 2 Extended+ that uses Fused Deposition Modelling (FDM) as AM technology. The values of the manufacturing parameters were set as follows: nozzle size equal to 0.4 mm, nozzle temperature to 240°C, build-plate temperature to 60°C, print speed to 30 mm/s, fill density to 100%, layer height to 0.1 mm, and shell thickness, t_s, equal to 0 mm, 0.4 mm, and to 0.8 mm.

As to the latter manufacturing parameter, Figs 4a, 4b and 4c show three examples of specimens fabricated by making t_s vary in the range 0-0.8 mm. In the 3D-printing ambit, the shell, also called "outline" or "outer perimeter", is the outer wall in an AM object. When 3D-printers start manufacturing a new layer, the shells are always the first parts that are made, so

that a kind of external "retaining wall" is created before the internal structure of the object is built up. The shell's thickness is typically a multiple of the nozzle diameter, with this preventing voids and manufacturing defects from being introduced in the AM object.

Turning back to the specimens being manufactured, Fig. 4a makes it evident that the absence of the shell (i.e., t_s=0 mm) resulted in samples having quite rough lateral surfaces. In contrast, setting the shell thickness, t_s, equal to either 0.4 mm (i.e., equal to the nozzle diameter) or 0.8 mm (that is, equal to two times the nozzle diameter) resulted in specimens all characterised by smooth lateral surfaces (Figs 4b and c).

As shown in Fig. 4d, all the samples were fabricated horizontally (i.e., flat on the build-plate) by making manufacturing angle θ_p vary in the range 0°-90°, with θ_p being the angle between reference printing direction y_p and the longitudinal axis of the specimens themselves. This allowed us to make specimens having different meso-structural features, since, independently of the value of angle θ_p, the extruded filaments used to build the bulk volume of the specimens were deposited, layer upon layer, always at ±45° to manufacturing direction y_p (Fig. 4d). In other words, if the orientation of the 3D-printed filaments with respect to the specimen axis is described by adopting the same terminology as the one which is usually used with fibre reinforced composite materials, according to Fig. 4d, a θ_p angle equal to 0° and to 90° resulted in a ±45° configuration, a θ_p angle equal to 30° in a -15°/+75° configuration and, finally, a θ_p angle equal to 45° in a 0°/+90° configuration.

The un-notched specimens (Fig. 2a), the samples weakened by crack-like notches (Fig. 2b) and the notched specimens (Fig. 3) had all thickness equal to 4 mm, whereas the C(T) specimens were manufactured, according to ASTM D5045–14 [24], by setting the thickness equal to 20 mm (Fig. 2c) and to 30 mm (Fig. 2d). The dimensions in the virtual models used as input information for the 3D-printer were set equal to the nominal values that are reported in the technical drawings of Figs 2 and 3. For each sample being fabricated and tested, Tables 1 to 7 list the values of the average dimensions as measured using a high-precision calliper and an optical microscope (refer to the Nomenclature for the definition of the adopted symbols). By contrasting the actual dimensions summarised in Tables 1 to 7 with the nominal dimensions of the specimens as shown in Figure 1, it is possible to observe that the manufacturing accuracy varied slightly with angle θ_p. The pictures reported in Figures 5a to 5e demonstrate that the 3D-printer being used allowed us to manufacture the different geometrical features being designed by always reaching an adequate level of geometrical/dimensional accuracy.

The plain samples (Fig. 2a), the specimens containing crack-like notches (Fig. 2b) and the rectangular plates with opposite U- and V-notches (Figs 3a to 3f) were tested under tensile loading. The specimens with single U- and V-notches (Figs 3g to 3m) were tested instead under three point bending. For the latter testing configuration, the span between the two lower

supports was set equal to 50 mm for the specimens of Figs 3g to 3i and to 60 mm for the samples containing single open notches (Figs 3k to 3m). Some pictures showing the different experimental set-ups that were used to generate the results summarised in Tables 1 to 7 are reported in Figs 4e to 4h. The C(T) specimens were tested according to the experimental procedure that is recommended in ASTM D5045-14 [24] (Fig. 4i). Independently of geometry and type of applied loading, all the samples were tested using a Shimadzu universal machine under a displacement rate equal to 2 mm/sec, with the local strain in the un-notched specimens being measured using an extensometer with gauge length equal to 50mm (Fig. 4e). To generate statistically-meaningful data, 3 tests were run for any geometry/loading configuration being investigated, with the tests being run up to the complete failure of the samples.

As far as notches are concerned, it is well-known that the notch opening angle, α, is one of those geometrical variables that affects the distribution of the local linear-elastic stress fields [25]. However, the effect of the opening angle can be neglected with little loss of accuracy as long as α is lower than about 100°. In contrast, for values of angle α larger than about 100° the opening angle influences markedly not only profile and magnitude of the local linear-elastic stress fields [26], but also notched components' overall strength [27]. In this context, it is also important to highlight that, as far as certain brittle materials are concerned, when opening angle α is equal to 100° the difference in terms of failure load between the crack-like case and the open notch case is seen to be of the order of 25%. These considerations explain way the specimens shown in Figs 3d to 3f as well as in Figs 3k to 3m were manufactured by setting the opening angle, α, equal to 135°.

To conclude, all the results that were generated according to the experimental protocols described in the present section are listed in Tables 1 to 7 (refer to the Nomenclature for the definition of the adopted symbols).

4. Mechanical behaviour

The stress vs. strain diagrams of Fig. 6 summarise the mechanical behaviour displayed by the investigated AM PLA, where the curves being reported were generated by testing, under tensile loading (Fig. 4e), the plain specimens sketched in Fig. 2a. With regard to the profile of these stress-strain curves, the charts of Fig. 6 make it evident that the mechanical response of the tested AM PLA was predominantly linear up to the maximum stress recorded during testing, with this holding true independently of shell thickness, t_s, and manufacturing angle, θ_p. In other words, according to the diagrams of Fig. 6 (whose validity is fully supported also by the experimental findings of Song et al. [12]), the stress vs. strain behaviour of the tested

AM material could be modelled as purely linear-elastic up to the UTS, with this assumption resulting just in a little loss of accuracy.

Turning to the non-linear part of the total deformation, the specimens manufactured by setting angle θ_p equal to 0° and 90° were seen to be characterised by a large level of tensile ductility. In contrast, for the samples with θ_p equal to 30°, 45°, and 60°, failures took place as soon as the applied stress reached its maximum value. It is worth pointing out here also that no necking was observed to occur prior failure, with this holding true independently of manufacturing angle and shell thickness.

In order to investigate quantitatively the mechanical behaviour of our AM PLA, the stress-strain curves of Fig. 6 were post-processed to determine, for any specimen being tested, Young's modulus, E, 0.2% proof stress, $\sigma_{0.2\%}$, and tensile strength, σ_{UTS}. The obtained results (listed also in Table 1) are summarised in the diagrams of Fig. 7 where, for a shell thickness, t_s, equal to 0, 0.4, and 0.8 mm, the experimental values of E (Fig. 7a), $\sigma_{0.2\%}$ (Fig. 7b), and σ_{UTS} (Fig. 7c) are plotted against manufacturing angle θ_p. These charts demonstrate that both angle θ_p and shell thickness t_s had little influence on the values measured for the three mechanical properties under investigation. However, even if a univocal trend is not evident, it is possible to say that, in general terms, E, $\sigma_{0.2\%}$, and σ_{UTS} tended to slightly increase as the shell thickness increased. As a consequence, since the variation of the mechanical properties with t_s was seen to be very little, the notched specimens were all manufactured by setting the thickness of the shell invariably equal to 0.4 mm. This was done also because, according to good practice in 3D-printing of polymeric materials, it is always advisable to set the shell thickness equal to the nozzle diameter. Another important aspect is that the mechanical behaviour for θ_p equal to 0° and 30° was markedly similar to that observed for θ_p equal to 60° and 90°, respectively (see Fig. 7). This explains the reason why the static strength of the notched specimens sketched in Fig. 3 was investigated by testing solely samples fabricated by setting manufacturing angle θ_p equal to 0°, 30°, and 45°. These considerations based on the mechanical response of the plain specimens allowed us to reduce the number of samples that needed to be tested in order to properly characterise the notch behaviour of the AM PLA being studied.

By assuming then that the effect of both θ_p and t_s is negligible, the mechanical properties averaged from the 45 tests being run took on the following values (see also Fig. 7): E=3479MPa, $\sigma_{0.2\%}$=41.7MPa, and σ_{UTS}=42.9 MPa. With regard to the average values determined for $\sigma_{0.2\%}$ and σ_{UTS}, it is important to point out that the difference between these two material properties was seen to be of the order of 2%. This further confirms that the stress vs. strain response of the AM PLA being investigated can be modelled as linear up to the UTS. According to this simplifying hypothesis, as far as the static assessment of AM PLA is

concerned, its mechanical behaviour can be described effectively without invoking the use of complex non-linear stress vs. strain relationships.

Turning back to the influence of manufacturing parameters t_s and θ_p, the graphs of Fig. 7 show that the mechanical properties determined by making θ_p vary in the range 0°-90° and t_s in the range 0-0.8 mm fall all within an error interval of $\pm 2S_D$, where S_D is the standard deviation characterising the statistical dispersion of any of the above mechanical properties. Having highlighted this important aspect, it is important to highlight that, certainly, from a materials science point of view, both the manufacturing angle and the shell thickness are seen to affect the overall mechanical response of AM PLA. However, the diagrams of Fig. 7 strongly support the idea that, from an engineering design viewpoint, the effect of t_s and θ_p on E, $\sigma_{0.2\%}$ and σ_{UTS} can be neglected with little loss of accuracy. This represents the fundamental assumption that will be made in Section 8 in order to extend the use of the TCD to the static assessment of notched AM PLA.

To conclude, it is interesting to observe that, for conventional neat PLA, E is seen to vary in the range 3200-4500 MPa, σ_y in the range 40-65 MPa and σ_{UTS} in the range 45-80 MPa [28-31]. In this context, it is important to highlight that the mechanical properties of commercial PLA depend on a large number of factors that include, amongst others, characteristics of the adopted manufacturing process, set values for the technological variables, molecular weight and crystallinity level [32]. Having said that, the average values for E, σ_y and σ_{UTS} reported in Fig. 7 suggest that FDM allows objects of PLA to be manufactured by obtaining mechanical properties that are very similar to those that are obtained via conventional manufacturing processes (such as, for instance, injection moulding). This result is certainly interesting and promising, especially in light of the fact that the advantage of AM over the other existing manufacturing technologies is that objects with complex shapes can be fabricated at a relatively low cost. At the same time, this result is somehow surprising since the material meso-structure characterising AM PLA is markedly different from the one that is observed in conventional neat PLA [30].

5. Notch static strength

The diagrams of Fig. 8 show some example of the force/moment vs. displacement curves that were generated by testing the notched specimens sketched in Figs 2b and 3 under tensile as well as under bending loading. In particular, Fig. 8 gives an overview of the static behaviour displayed by the tested notched specimens, with the reported curves being those from the first test that was run for any geometry/loading configuration being investigated. The results obtained under tensile loading show that the force vs. displacement curves of the notched specimens were all characterised by an evident bi-linear trend. In more detail, an initial linear

branch was always followed by second linear branch characterised by a slightly lower slope, with the change in the gradient occurring, independently of the notch profile, around 0.5 mm. Turning to the results generated under three-point bending, the charts of Fig. 8 confirm that, as expected, the resulting moment vs. vertical displacement curves were all characterised by an initial non-linear part, with this non-linear behaviour being due to the physiological adjustment of the testing apparatus. This non-linear branch was then followed by a predominantly linear behaviour up to final breakage, with this holding true both for U-notches and for open notches.

In order to study the notch behaviour of the investigated AM PLA, initially, we post-processed the results generated by testing, under tensile loading, the specimens containing crack-like notches (Fig. 2b). These samples were manufactured by making t_s vary in the range 0-0.8mm and θ_p in the range 0°-90°. Same examples showing the profile of the manufactured V-notches are shown in Fig. 5a for t_s equal to 0, 0.4, and 0.8mm. The generated results are summarised in the nominal net failure stress, σ_f, vs. manufacturing angle, θ_p, diagram of Fig. 9a (see also Tab. 2). According to this chart, for θ_p equal to 30° and 60° the static strength increased with the increase of the shell thickness. In contrast, the results generated by setting angle θ_p equal to 0°, 45° and 90° show no clear trend.

As discussed in the previous section, the shell thickness was seen to have little effect on the static strength of the AM PLA being tested. Accordingly, the notched samples sketched in Fig. 3 were all manufactured by setting t_s invariably equal to 0.4 mm (i.e., equal to the nozzle diameter), with angle θ_p being equal to 0°, 30°, and 45°.

The σ_f vs. θ_p diagrams reported in Figs 9b to 9e summarise the results generated by testing both U-notches and open notches under tension as well as under three-point bending (see also Tables 3 to 6), where r_n is used to denote the notch root radius. These charts make it evident that, in contrast with the mechanical behaviour displayed by the plain and sharply V-notched specimens, the manufacturing angle did affect the overall strength of the tested notched samples, with this holding true especially under three point bending (Figs 9d and 9e). In particular, for the specimens loaded in bending, the obtained trends suggest that the static strength tended to decrease as angle θ_p increased. Another important aspect is that, given the type of loading, the sharpest notches did not always result in the lowest static strength. This unexpected behaviour can clearly be seen by observing the trends of the results generated, under tension, by testing the U- (Fig. 9b) and sharply V-notched specimens (Fig. 9c) manufactured by setting angle θ_p equal to 30°.

To conclude, it is worth observing that the straight horizontal lines plotted in the diagrams of Figs 9b to 9e were determined by averaging, for any value of the notch root radius, r_n, the results obtained by testing specimens with θ_p equal to 0°, 30°, and 45°. Owing to the complex

notch behaviour shown by the different samples being tested, such lines were reported to show, in a simplified way, the general trends and not to model the effect of the manufacturing angle on the notch strength of the AM PLA being investigated.

6. Cracking behaviour

In order to understand the influence of both the shell thickness, t_s, and the manufacturing angle, θ_p, on the cracking behaviour of the 3D-printed PLA being investigated, initially attention was focused on the crack paths resulting in the final breakage of the plain specimens. By considering both the crack initiation and the crack propagation phases, the matrix of failures reported in Fig. 10 summarises the fracture surfaces that were observed in the un-notched samples loaded in tension. In particular, the cracks were seen to initiate, in the gauge length area, on planes that were almost perpendicular to the direction along which the tensile force was applied, with this holding true independently of manufacturing angle, θ_p, and thickness of the superficial shell, t_s. This opening-mode dominated initiation phase resulted in embryonic cracks having length of the order of 0.25mm in the specimens with t_s=0 mm and of the order of the shell thickness in the samples manufactured by setting t_s equal to 0.4mm and to 0.8mm (Fig. 10). The subsequent propagation process was seen to occur along zig-zag paths that followed the directions of the deposited filaments forming the bulk material of the specimens. The profile of the observed crack paths strongly supports the idea that, irrespective of manufacturing angle and shell thickness, the propagation phase was the result of two dominant failure mechanisms, i.e., de-bonding between adjacent filaments and rectilinear cracking of the filaments themselves (Fig. 10).

Fig. 11 shows the crack initiation phase as it was observed in the specimens containing crack-like notches (Fig. 2b). With regard to the samples with t_s=0 mm, it is important to observe here that they were fabricated by cutting the material using a sharp thin knife, with this simple manufacturing process resulting in an average length of the notch root radius equal to about 0.05mm (see also Fig. 5a). In contrast, the specimens with t_s equal to 0.4mm and to 0.8mm were fabricated by setting the notch root radius equal to zero in the virtual models used as input information for the 3D-printer. The pictures of Fig. 11 suggest that, due to the sharpness of the notches, there was no clear initiation phase, with the profiles of the crack paths being governed by the orientation of the deposited filaments (i.e., by angle θ_p). This strongly supports the idea that in the specimens containing crack-like notches as well the fracture process was due to the combined effect of de-bonding and rectilinear cracking. Another important aspect is that, in some of the specimens with t_s equal to 0.4 mm and to 0.8 mm, the cracks were seen to initiate on the flank of the notch, i.e., slightly away from the notch tip - see, for instance, the failures in the cases with θ_p equal to 45° and 90° for the specimens with t_s=0.4mm (Fig. 11). This can be ascribed to a technological limitation of the adopted 3D-

printer that resulted in a defective adhesion between the shell and the filler material in the vicinity of some of the crack-like notches that were manufactured.

Figs 12 and 13 show the crack initiation regions in the notched specimens loaded in tension and in three-point bending, respectively. Similar to what was observed in the plain specimens (Fig. 10), the cracks were seen to initiate at the notch tips on planes that were almost normal to the direction experiencing the maximum opening stress, with this holding true independently of type of loading, sharpness of the notch, and opening angle. These initial cracks were seen to grow up to a distance from the notch tip equal to about 0.4mm (i.e., of the order of the shell thickness). The subsequent propagation followed instead a zig-zag path whose profile depended on the morphology of the bulk material as obtained by changing the value of manufacturing angle θ_p. Accordingly, the hypothesis can be formed that also in the notched specimens the propagation phase occurred due to combined de-bonding and rectilinear cracking.

7. Fracture toughness

In order to investigate the characteristics of the fracture toughness of the AM PLA being studied, initially, the results generated by testing, under tensile loading, the specimens containing crack-like notches (Fig. 2b) were post processed to determine K_c for t= 4 mm. The obtained results are listed in Table 2 and summarised in the K_c vs. θ_p diagram of Figure 14a, with the required LEFM shape factor being estimated using the classic formula reported in Ref. [33]. According to Figure 14a, it is possible to say that, as a general trend, the fracture toughness tended to increase slightly with the increase of the shell thickness, t_s. The chart of Figure 14a also shows that, as expected, manufacturing angle θ_p did affect the value of K_c determined for t=4 mm. This is because, as already discussed in Section 6, the cracks in the specimens containing crack-like notches were seen to propagate by following zig-zag paths whose profiles depended on the orientation of the deposited filaments. In other words, while, at a microscopic level, the cracks were all seen to propagate along the notch bisector, at a mesoscopic level the growth occurred instead due to local Mixed-Mode I/II mechanisms. Solely in the specimens manufactured by setting θ_p=45° the cracks were driven by pure Mode I mechanisms also at a mesoscopic level. This was a consequence of the fact that, in these specimens, the deposited filaments were either parallel or perpendicular to the direction along which the loading was applied. However, in spite of the complexities characterising the observed fracture behaviour, the chart of Figure 14a shows that all the experimental results being generated fell within two standard deviations of the mean, with the average value for K_c being equal to 3.5 MPa·m$^{1/2}$.

Subsequently, the fracture toughness for the investigated AM PLA was attempted to be determined, as recommended in ASTM D5045-14 [24], by testing also C(T) specimens with

thickness, t, equal to 20 mm (Fig. 2c). These samples were manufactured by setting t_s invariably equal to 0.4 mm. The obtained results are summarised both in Table 7 and in the K_c vs. θ_p diagram of Figure 14b. In particular, the graph of Figure 14b suggests that also the values of the fracture toughness determined via the C(T) specimens with t=20 mm were slightly affected by manufacturing angle θ_p, even though all the results are still within two standard deviations of the mean. In contrast with the cracking behaviour observed in the specimens with crack-like notches, the propagation of the cracks in the C(T) samples was influenced instead by the orientation of the deposited filaments, with this holding true at both a mesoscopic and a macroscopic level (see Figs 14c to 14e). In particular, in the specimens manufactured by setting θ_p equal to 0° and 30°, the growth process was mixed-mode governed (Figs 14c and 14d), whereas in the specimens with θ_p=0° it was instead driven by pure Mode I mechanisms (Fig. 14e). Another important aspect being evidenced by the pictures reported in Figs 14c to 14e is that the cracks were seen to initiate slightly away from the notch tip, with the initial growth following the profile of the shell filament used to build the surface of the crack-like notches themselves. As to this aspect, it is important to point out that, contrary to what is recommended in ASTM D5045-14 [24], no pre-cracks were introduced in the specimens. This was done intentionally to try to determine the fracture toughness for the AM PLA under investigation by taking into account also the effect of the shell thickness.

Taking advantage of to the results summarised in Figs 14, the thickness of the C(T) specimens was then increased up to 30mm in order to determine the plane strain fracture toughness, K_{Ic}, of the AM PLA under investigation. In this case, to promote a crack propagation process that was purely governed by Mode I mechanisms, the samples were manufactured by setting θ_p invariably equal 45° (with t_s being again equal to 0.4mm). The diagram of Fig. 15a shows the force vs. displacement curves that were obtained by testing these specimens, with the results being reported in Table 7. In particular, the K_{Ic} values extrapolated according to the ASTM D5045-14 procedure [24] and listed in Table 7 were remarkably consistent, with the plane strain fracture toughness being invariably equal to 3.7 MPa·m$^{1/2}$. The pictures of Fig. 15b confirm that, as planned, the propagation was purely Mode I governed, with the initiation occurring again slightly away from the notch tip.

The average values for the fracture toughness that were determined according to the different experimental strategies summarised in the present section confirm that K_c was markedly influenced not only by the thickness, but also by the geometry of the specimens being used. In particular, in contrast with what is usually observed in conventional engineering materials, the fracture toughness did not increase gradually as the specimen thickness increased. In fact, the average value of K_c for t equal to 4 mm was seen to be lower than the corresponding average values determined both for t equal to 20 mm and for t equal to 30 mm. This is very surprising especially because, according to the classic rule recommended in the pertinent ASTM standard

[22], the value for K_c obtained with t=30 mm was generated under fully-developed plane strain conditions.

Another important aspect that is worth being pointed out is that the plane strain fracture toughness for conventional neat PLA is seen to vary in the range 2-4 MPa·m$^{1/2}$, with K_{Ic} increasing as the percentage of crystallinity increases [32]. Therefore, since the plane strain fracture toughness for the AM PLA under investigation was measured to be equal to 3.7 MPa·m$^{1/2}$ (Tab. 7), it is evident that the use of FDM allowed us to produce a material having a resistance to fracture similar to the one characterising commercial neat PLA fabricated using conventional manufacturing techniques.

To conclude, it is possible to say that, clearly, more work needs to be done in order to better understand the existing interactions between manufacturing variables and geometry/thickness of the specimens so that the use of the classic LEFM concepts can be extended safely to the static design of AM PLA containing cracks.

8. TCD's accuracy in estimating static strength of notched 3D-printed PLA

The ultimate goal of the present investigation is to promote a simple methodology that can be used in situations of practical interest to design notched components of AM PLA against static loading. Clearly, modelling the markedly complex notch/cracking behaviour displayed by the AM PLA being investigated represents a challenging task for the TCD. Such an intrinsic complexity suggests that forming a number of simplifying hypotheses is the only way to try to use this theory (as reviewed in Section 2) to address this intractable problem. These assumptions will be discussed in what follows.

According to the diagrams of Figure 7, both θ_p and t_s are seen to affect the overall mechanical behaviour of the investigated AM PLA. In spite of this experimental evidence, the initial hypothesis can be formed that the 3D-printed PLA under investigation behaves like a homogenous and isotropic material. This assumption can be made because, as shown in Figure 7, the experimental values of E, $\sigma_{0.2\%}$ and σ_{UTS} are all within two standard deviations of the mean. In other words, the diagrams of Fig. 7 suggest that, from an engineering point of view, the effect of manufacturing variables θ_p and t_s can be neglected with little loss of accuracy.

The second simplification being introduced to use the TCD is that the mechanical behaviour of the tested AM PLA is assumed to obey a simple linear-elastic constitutive law. The validity of this second hypothesis is strongly supported by the fact that, independently of angle θ_p and thickness t_s, the stress vs. strain response of the tested plain specimens is seen to be predominantly linear up to the maximum stress recorded during testing (see Fig. 6).

The most important implication of this assumption is that the TCD inherent material strength can be taken invariably equal to the UTS. In other words, since the mechanical behaviour of

the tested material can be linearized without much loss of accuracy, the AM PLA under investigation can be thought of as a brittle material for which $\sigma_o=\sigma_{UTS}$ [1, 6].

In line with the simplifying hypotheses discussed above, the local stress fields required to determine the TCD effective stress, σ_{eff}, were estimated by post-processing the results from simple linear-elastic bi-dimensional models solved using commercial FE software ANSYS®. The notched samples of Figure 3 were modelled by using bi-dimensional elements Plane183, where, for any notched geometry, the mapped mesh was gradually refined in the vicinity of the stress raiser apex until convergence occurred. In these models the material was set to be homogenous and isotropic.

In order to attempt to use the TCD to estimate the static strength of the notched specimens being tested, the last problem to be addressed is the determination of critical distance L for the AM material under investigation. Unfortunately, owing to the issues associated with the determination of K_{Ic} as discussed in detail in Section 7, it was not possible for definition (5) to be used to estimate L directly. To overcome this problem, a strategy similar to the one described in Figure 1e was followed, the advantage in this case being that σ_o could be assumed to be invariably equal to σ_{UTS}. In particular, as shown in the stress vs. distance diagram of Figure 16a, initially the local linear-elastic stress fields were determined, in the incipient failure condition, by post-processing the results generated by testing, under tension, the sharply U-notched specimens (see Fig. 3a and Tab. 3). The three stress-distance curves reported in Fig. 16a were determined by averaging the three results from the three tests that were run for any value of the manufacturing angle, θ_p, being investigated (i.e., θ_p=0°, 30°, 45°). Finally, according to the Point Method's *modus operandi*, critical distance L was determined by averaging the distance resulting from the three points of intersection between the straight horizontal line modelling the plain material UTS and the three stress-distance curves describing the local stress fields in the notched specimens used as calibration information. As shown in Fig. 16a, this simple procedure resulted in an average value of the critical distance equal to 4.6 mm. Therefore, L=4.6 mm and $\sigma_o=\sigma_{UTS}$=42.9 MPa were used to assess the accuracy of the TCD against the experimental results summarised in Tables 3 to 6.

It is interesting to recall here that, in the TCD framework, engineering materials' strength is supposed to depend on the stress acting, in the vicinity of the crack initiation locations, on a finite portion of material. In this setting, the size of this process zone is seen to be directly related to length L [1, 34]. Critical distance L depends in turn on the size of the dominant source of microstructural heterogeneity characterising the material being assessed [34, 35]. For the AM PLA being investigated in the present study, the inherent microstructural heterogeneity can specifically be related to the size of the 3D-printed filaments which was of the order of 0.4 mm (i.e., approximately equal to the nozzle size). In a recent investigation, Taylor [36] has argued that the L value for engineering materials is, in general, about an order

of magnitude larger than the size of the dominant microstructural features. These arguments seem to strongly support the idea that the characteristic length suitable for assessing the static strength of the AM PLA being tested was closely related to the size of the extruded filaments, with L being, as observed by Taylor [36], ten times larger than the diameter of the AM filaments themselves. From a static strength point of view, such a large value for L suggests that the material being considered is characterised by a relatively low notch sensitivity, the validity of this observation being fully supported by the experimental results summarised in Tabs 2 to 6. Another interesting aspect is that, owing to the difficulties associated with the determination of critical distance L for the AM material being investigated, one may attempt to use either Finite Fracture Mechanics [37] or the Strain Energy Density approach [38] to determine a suitable material characteristic length.

Turning back to the validation exercise summarised in the present section, having estimated L, the local linear-elastic stress fields determined numerically were then used to estimate according to both the Point, Eq. (3), and the Area Method, Eq. (1), the effective stress in the incipient failure condition for the different geometrical features/loading configurations being investigated. Unfortunately, it was not possible for us to check the accuracy of the TCD applied in the form of the Line Method, Eq. (2), simply because the length of the linear integration domain (i.e., 2L=9.2 mm) was larger than half width of the tested specimens [1].

The diagrams of Figure 16b and 16c summarise the overall accuracy that was obtained by applying the Point and the Area Method, respectively, to estimate the static strength of the notched specimens sketched in Figure 3. In these diagrams, the error was calculated as follows:

$$\text{Error} = \frac{\sigma_{\text{eff}} - \sigma_{\text{UTS}}}{\sigma_{\text{UTS}}}[\%] \tag{1}$$

According to the above definition, a positive error is associated with estimates that are conservative, whereas, a negative error denotes estimates that are non-conservative.

The diagrams of Figure 16b and 16c demonstrate that, in spite of the complex mechanical/cracking behaviour characterising the AM PLA under investigation, the TCD is remarkably accurate in predicting the static strength of the notched specimens being tested, with its systematic usage resulting in estimates falling mainly within an error interval of ±20%. From a static design viewpoint, this level of accuracy is certainly acceptable since, as far as conventional engineering materials are concerned, it is not possible to distinguish between an error of ±20% and an error of 0% due to the problems which are usually encountered during testing as well as during the numerical analyses [1].

To conclude, it can be said that the validation exercise discussed in the present section strongly supports the idea that the simple linear-elastic TCD can be used in situations of practical interest to design notched components of AM PLA against static loading. In this context, the key feature of the TCD is that it can be applied by directly post-processing the results from linear-elastic FE models done by treating the material as homogenous and isotropic. The key advantage of this *modus operandi* is that the same numerical models can be used to not only perform the geometrical/shape optimisation of the component being designed, but they can also be used as input information for the manufacturing process.

9. Conclusions

The present paper investigates the accuracy of the classic linear-elastic TCD in designing notched AM PLA against static loading. In order to consistently extend the use of this theory to the static assessment of 3D-printed PLA wakened by stress raisers of different sharpness, the mechanical/cracking behaviour of the specific AM material being studied is investigated in detail by considering the effect of manufacturing angle and shell thickness. The accuracy and reliability of the TCD is checked against a large number of experimental results generated by testing, under both tensile and bending loading, specimens of AM PLA containing different geometrical features (open notches included).

With regard to the specific 3D-printed PLA/manufacturing technology being considered in the present investigation, the most relevant conclusions are as follows:

- independently of manufacturing angle θ_p and shell thickness t_s, the mechanical behaviour can be model as linear-elastic up to the UTS;
- as both θ_p and t_s vary, E, $\sigma_{0.2\%}$ and σ_{UTS} are seen to be within two standard deviations of the mean;
- the sharpest geometrical features does not always result in the lowest static strength;
- the cracking behaviour is governed by the orientation of the deposited filaments;
- the fracture toughness value of the AM material being investigated is strongly affected not only by the thickness, but also by the geometry of the specimens being used to determine this LEFM mechanical property;
- the TCD is seen to be highly accurate in estimating notch static strength, with its use returning estimates falling mainly within an error interval of ±20%;
- the TCD can be applied by taking inherent strength σ_o invariably equal to σ_{UTS};
- the TCD critical distance, L, is recommended to be estimated by post-processing the results generated by testing specimens containing a known sharp geometrical feature;
- more work needs to be done in order to: (i) understand the existing interactions amongst fracture toughness, manufacturing parameters, geometry/thickness of the

specimens, and type of applied loading; (ii) check the accuracy of the TCD in estimating static strength of notched PLA subjected to multiaxial loading.

References

[1] D. Taylor, The Theory of Critical Distances: A New Perspective in Fracture Mechanics, Elsevier Ltd, Oxford, UK, 2007.

[2] L. Susmel, D. Taylor, The theory of critical distances to estimate the static strength of notched samples of Al6082 loaded in combined tension and torsion. Part I: material cracking behaviour, Eng. Fract. Mech. 77 (2010) 452–469.

[3] L. Susmel, D. Taylor, The theory of critical distances to estimate the static strength of notched samples of Al6082 loaded in combined tension and torsion. Part II: multiaxial static assessment, Eng. Fract. Mech. 77 (2010) 470–478.

[4] Li, W., Susmel, L., Askes, H., Liao, F., Zhou, T. Ductile fracture of Q460 steel: application of the Theory of Critical Distances. Eng. Fail. Anal. 70 (2016) 73–89.

[5] L. Susmel, D. Taylor, On the use of the theory of critical distances to predict static failures in ductile metallic materials containing different geometrical features, Eng. Fract. Mech. 75 (2008) 4410–4421.

[6] L. Susmel, D. Taylor, The theory of critical distances to predict static strength of notched brittle components subjected to mixed-mode loading, Eng. Fract. Mech. 75 (2008) 534–550.

[7] A.A.H. Ameri, J.B. Davison, L. Susmel, On the use of linear-elastic local stresses to design steel arc welded joints against static loading, Eng. Fract. Mech. 136 (2015) 38-57.

[8] R. Louks, H. Askes, L. Susmel, A simplified reformulation of the Theory of Critical Distances for rapid finite element design of notched materials against static loading, Mater. Des. 108 (2016) 769-779.

[9] J.D. Ciurana, Selecting process parameters in RepRap additive manufacturing system for PLA scaffolds manufacture, Procedia CIRP 5 (2013) 152-157.

[10] A. Lanzotti, M. Grasso, G. Staiano, M. Martorelli, The impact of process parameters on mechanical properties of parts fabricated in PLA with an open-source 3-D printer, Rapid Prototyping J. 21 5 (2015) 604-617.

[11] J.M. Chacón, M.A. Caminero, E. García-Plaza, P.J. Núñez, Additive manufacturing of PLA structures using fused deposition modelling: Effect of process parameters on mechanical properties and their optimal selection, Mater. Des. 124 (2017) 143-157.

[12] Y. Song, Y. Li, W. Song, K. Yee, K.-Y. Lee, V.L. Tagarielli, Measurements of the mechanical response of unidirectional 3D-printed PLA, Mater. Des. 123 (2017) 154-164.

[13] C. Casavola, A. Cazzato, V. Moramarco, C. Pappalettere, Orthotropic mechanical properties of fused deposition modelling parts described by classical laminate theory, Mater. Des. 90 (2016) 453-458.

[14] B. Wittbrodt, J.M. Pearce, The effects of PLA color on material properties of 3-D printed components, Additive Manufacturing 8 (2015) 110-116.

[15] D. Bellett, D. Taylor, S. Marco, E. Mazzeo, J. Guillois, T. Pircher, The fatigue behaviour of three-dimensional stress concentrations. Int. J. Fatigue 27 (2005) 207-221.

[16] D. Taylor, Geometrical effects in fatigue: a unifying theoretical model. Int. J. Fatigue 21 (1999) 413-420.

[17] L. Susmel, Multiaxial Notch Fatigue: from nominal to local stress-strain quantities. Woodhead & CRC, Cambridge, UK, 2009.

[18] L. Susmel, A unifying approach to estimate the high-cycle fatigue strength of notched components subjected to both uniaxial and multiaxial cyclic loadings. Fatigue Fract. Engng. Mater. Struct. 27 (2004) 391-411.

[19] J.M. Whitney, R.J. Nuismer, Stress Fracture Criteria for Laminated Composites Containing Stress Concentrations. J. Compos. Mater. 8 (1974) 253-65.

[20] D. Taylor D, Predicting the fracture strength of ceramic materials using the theory of critical distances. Eng. Fract. Mech. 71 (2004) 2407-2416.

[21] D. Taylor, M. Merlo, R. Pegley, M.P. Cavatorta, The effect of stress concentrations on the fracture strength of polymethylmethacrylate. Mater. Sci. Eng. A382 (2004) 288–294.

[22] R. Negru, L. Marsavina, T. Voiconi, E. Linul, H. Filipescu, G. Belgiu, Application of TCD for brittle fracture of notched PUR materials. Theor. Appl. Fract. Mec. 80-A (2015) 87-95.

[23] R. Negru, L. Marsavina, H. Filipescu, C. Căplescu, T. Voiconi, Assessment of brittle fracture for PUR materials using local strain energy density and theory of critical distances, Theor. Appl. Fract. Mec. 79(2015) 62-69.

[24] ASTM D5045-14, Standard Test Methods for Plane-Strain Fracture Toughness and Strain Energy Release Rate of Plastic Materials, ASTM International, West Conshohocken, PA, 2014, www.astm.org.

[25] B. Atzori, P. Lazzarin, R. Tovo, Stress field parameter to predict the fatigue strength of notched components. J. Strain Anal. Eng. 34 (1999) 437-453.

[26] P. Lazzarin, R. Tovo, A unified approach to the evaluation of linear elastic stress fields in the neighbourhood of cracks and notches. Int. J. Fracture 78 (1996) 3-19.

[27] L. Susmel, D. Taylor, R. Tovo, On the estimation of notch fatigue limits by using the Theory of Critical Distances: L, a_0 and open notches. Structural Durability and Health Monitoring 4 (2008) 1-18.

[28] D. Garlotta, A Literature Review of Poly(Lactic Acid). J. Polym. Environ. 9 (2001) 63-84.

[29] M. Jamshidian, E. Arab-Tehrany, M. Imran, M. Jacquot, S. Desobry, Poly-Lactic Acid: Production, Applications, Nanocomposites, and Release Studies. Compr. Rev. Food Sci. Food Saf. 9 (2010) 552–571.

[30] F. Carrasco, P. Pagès, J. Gámez-Pérez, O.O. Santana, M.L. Maspoch, Processing of poly(lactic acid): Characterization of chemical structure, thermal stability and mechanical properties. Polym. Degrad. Stab. 95 (2010) 116-125.

[31] S. Farah, D. G. Anderson, R. Langer, Physical and mechanical properties of PLA, and their functions in widespread applications — A comprehensive review. Adv. Drug Deliv. Rev. 107 (2016) 367–392.

[32] S.-D. Park, M. Todo, K. Arakawa, Effects of isothermal crystallization on fracture toughness and crack growth behavior of poly (lactic acid). J. Mater. Sci. 40 (2 005) 1055 – 1058

[33] H. Tada, P.C. Paris, G.R. Irwin, Stress Analysis of Cracks Handbook, ASME Press, USA, 2000.

[34] H. Askes, L. Susmel, Understanding cracked materials: is Linear Elastic Fracture Mechanics obsolete? Fatigue Fract. Engng. Mater. Struct. 38(2) (2015) 154-160.

[35] C. Bagni, H. Askes, L. Susmel, Gradient elasticity: a transformative stress analysis tool to design notched components against uniaxial/multiaxial high-cycle fatigue. Fatigue Fract. Engng. Mater. Struct. 39(8) (2016) 1012-1029.

[36] D. Taylor, The Theory of Critical Distances: A link to micromechanisms. Theor. Appl. Fract. Mec. 90 (2017) 228–233

[37] P. Cornetti, N. Pugno, A. Carpinteri, D. Taylor, Finite fracture mechanics: A coupled stress and energy failure criterion. Eng. Fract. Mech. 73 (2006) 2021-2033.

[38] M. R. Ayatollahi, M. Rashidi Moghaddam, F. Berto, A generalized strain energy density criterion for mixed mode fracture analysis in brittle and quasi-brittle materials. Theor. Appl. Fract. Mec. 79 (2015) 70-76.

List of Captions

Tables

Code	θ_P	t_s	w_n	t	F_f	E	$\sigma_{0.2\%}$	σ_{UTS}
	[°]	*[mm]*	*[mm]*	*[mm]*	*[N]*	*[MPa]*	*[MPa]*	*[MPa]*
nsP_0_1	0	0	15.25	4.13	2828	3538	44.1	44.9
nsP_0_2	0	0	15.00	4.07	2839	3597	46.3	46.5
nsP_0_3	0	0	14.93	4.18	2853	3504	45.5	45.7
nsP_30_1	30	0	15.11	4.20	2536	3680	39.3	40.0
nsP_30_2	30	0	15.03	4.09	2522	3787	40.8	41.0
nsP_30_3	30	0	14.95	4.08	2500	3662	40.4	41.0
nsP_45_1	45	0	14.98	4.17	2479	3569	39.1	39.7
nsP_45_2	45	0	14.92	4.15	2453	3554	38.6	39.6
nsP_45_3	45	0	14.99	4.22	2385	3415	36.8	37.7
nsP_60_1	60	0	15.16	4.14	2385	3487	37.3	38.0
nsP_60_2	60	0	15.11	4.16	2408	3484	37.7	38.3
nsP_60_3	60	0	15.11	4.15	2400	3529	37.6	38.3
nsP_90_1	90	0	15.14	4.20	2597	3434	39.6	40.8
nsP_90_2	90	0	15.19	4.20	2635	3435	40.3	41.3
nsP_90_3	90	0	15.15	4.21	2622	3520	39.9	41.1
P_0_2	0	0.4	14.95	4.08	2527	3189	40.9	41.5
P_0_3	0	0.4	14.93	4.07	2613	3265	42.2	43.1
P_0_4	0	0.4	14.97	4.21	2734	3251	42.0	43.4
P_30_1	30	0.4	14.85	4.11	2302	3136	35.1	37.7
P_30_2	30	0.4	15.09	4.11	2528	3450	40.1	40.8
P_30_3	30	0.4	14.92	4.04	2667	3357	40.3	44.2
P_45_1	45	0.4	14.87	4.09	2614	3426	38.6	42.9
P_45_2	45	0.4	15.15	4.07	2621	3342	40.7	42.5
P_45_3	45	0.4	15.03	4.04	2554	3348	39.1	42.1
P_60_1	60	0.4	15.06	4.13	2465	3180	-	39.6
P_60_2	60	0.4	15.06	4.18	2574	3251	40.1	40.9
P_60_3	60	0.4	15.00	4.08	2577	3235	40.1	42.1
P_90_1	90	0.4	15.16	3.99	2814	3421	42.4	46.5
P_90_2	90	0.4	14.95	3.98	2855	3399	42.3	48.0
P_90_3	90	0.4	15.10	4.15	2678	3193	40.7	42.8
8P_0_1	0	0.8	15.22	4.25	2679	3369	37.2	41.4
8P_0_2	0	0.8	15.16	4.22	2702	3438	41.8	42.2
8P_0_3	0	0.8	15.19	4.17	2765	3540	42.8	43.6
8P_30_1	30	0.8	15.22	4.19	2425	3530	-	38.0
8P_30_2	30	0.8	15.22	4.20	2862	3651	44.7	44.8
8P_30_3	30	0.8	15.19	4.17	2807	3609	44.2	44.3
8P_45_1	45	0.8	15.07	4.06	2750	3778	44.5	45.0
8P_45_2	45	0.8	15.17	4.09	2881	3710	46.1	46.4
8P_45_3	45	0.8	15.09	4.14	2900	3688	46.0	46.4
8P_60_1	60	0.8	15.05	4.20	2851	3597	44.6	45.1
8P_60_2	60	0.8	15.03	4.28	2956	3578	45.5	45.9
8P_60_3	60	0.8	15.02	4.28	2882	3607	44.7	44.8
8P_90_1	90	0.8	15.14	4.23	3215	3584	47.9	50.2
8P_90_2	90	0.8	15.09	4.20	3210	3681	48.2	50.6
8P_90_3	90	0.8	15.13	4.24	3198	3573	47.7	49.8

Table 1. Summary of the experimental results generated by testing under tensile loading the un-notched specimens (Fig. 2a).

Code	θ_P	t_s	α	w_n	w_g	t	F_f	σ_f	K_C
	[Deg]	*[mm]*	*[Deg]*	*[mm]*	*[mm]*	*[mm]*	*[N]*	*[MPa]*	*[MPa·m$^{1/2}$]*
C_0_1	0	0	0	16.59	25.03	4.22	2999	45.3	3.9
C_0_2	0	0	0	16.38	24.78	4.20	2878	43.2	3.7
C_0_3	0	0	0	16.29	24.73	4.22	2924	43.2	3.7
C_30_1	30	0	0	16.56	24.98	4.21	2209	34.4	2.9
C_30_2	30	0	0	16.62	24.98	4.18	1973	30.4	2.6
C_30_3	30	0	0	16.56	24.92	4.18	2207	34.2	2.9
C_45_1	45	0	0	16.61	24.93	4.16	2386	37.0	3.2
C_45_2	45	0	0	16.54	24.90	4.18	2273	36.0	3.1
C_45_3	45	0	0	16.56	24.88	4.16	2216	35.1	3.0
C_60_1	60	0	0	16.47	24.83	4.18	2139	32.8	2.8
C_60_2	60	0	0	16.52	24.80	4.14	2026	32.3	2.8
C_60_3	60	0	0	16.66	24.82	4.08	2079	33.4	2.9
C_90_1	90	0	0	16.98	25.06	4.04	2616	41.6	3.6
C_90_2	90	0	0	16.84	25.06	4.11	2600	44.3	3.8
C_90_3	90	0	0	16.58	24.74	4.08	2863	46.9	4.0
sC_0_1	0	0.4	30	16.37	24.79	4.21	3003	43.8	3.8
sC_0_2	0	0.4	30	16.25	24.77	4.26	2946	42.2	3.6
sC_0_3	0	0.4	30	16.36	24.76	4.20	2996	43.4	3.7
sC_30_1	30	0.4	30	16.52	24.88	4.18	2839	41.0	3.5
sC_30_2	30	0.4	30	16.44	24.88	4.22	2823	40.6	3.5
sC_30_3	30	0.4	30	16.5	24.92	4.21	2626	37.4	3.2
sC_45_1	45	0.4	30	16.45	24.89	4.22	2389	33.7	2.9
sC_45_2	45	0.4	30	16.44	24.90	4.23	2426	34.4	3.0
sC_45_3	45	0.4	30	16.5	24.90	4.20	2369	33.9	2.9
sC_60_1	60	0.4	30	16.42	24.82	4.20	2556	37.2	3.2
sC_60_2	60	0.4	30	16.48	24.84	4.18	2512	37.1	3.2
sC_60_3	60	0.4	30	16.47	24.83	4.18	2503	36.6	3.1
sC_90_1	90	0.4	30	16.52	24.92	4.20	2960	43.6	3.7
sC_90_2	90	0.4	30	16.52	24.90	4.19	2973	43.5	3.7
sC_90_3	90	0.4	30	16.44	24.88	4.22	2928	42.9	3.7
8C_0_1	0	0.8	30	16.36	24.76	4.20	3064	44.4	3.8
8C_0_2	0	0.8	30	16.32	24.70	4.19	3099	45.3	3.9
8C_0_3	0	0.8	30	16.42	24.74	4.16	3083	45.9	3.9
8C_30_1	30	0.8	30	16.67	25.03	4.18	2982	43.6	3.8
8C_30_2	30	0.8	30	16.59	24.99	4.20	2968	43.3	3.7
8C_30_3	30	0.8	30	16.68	25.04	4.18	3067	45.4	3.9
8C_45_1	45	0.8	30	16.37	24.81	4.22	3133	45.4	3.9
8C_45_2	45	0.8	30	16.48	24.86	4.19	3161	46.5	4.0
8C_45_3	45	0.8	30	16.24	24.64	4.20	3115	45.1	3.8
8C_60_1	60	0.8	30	16.48	24.56	4.04	2900	44.7	3.8
8C_60_2	60	0.8	30	16.8	24.88	4.04	2868	43.8	3.8
8C_60_3	60	0.8	30	16.76	24.84	4.04	2846	43.9	3.8
8C_90_1	90	0.8	30	16.84	24.90	4.03	3297	50.3	4.3
8C_90_2	90	0.8	30	16.81	24.95	4.07	3307	49.6	4.3
8C_90_3	90	0.8	30	16.82	24.96	4.07	3268	49.5	4.3

Table 2. Summary of the experimental results generated by testing under tensile loading the specimens containing crack-like notches (Fig. 2b)

Code	θ_P	t_s	r_n	w_n	w_g	t	F_f	σ_f
	[°]	*[mm]*	*[mm]*	*[mm]*	*[mm]*	*[mm]*	*[N]*	*[MPa]*
S04_0_1	0	0.4	0.51	15.32	24.90	4.21	3234	50.1
S04_0_2	0	0.4	0.50	15.39	24.98	4.25	3212	49.1
S04_0_3	0	0.4	0.52	15.32	24.99	4.23	3218	49.7
S04_30_1	30	0.4	0.49	15.34	24.90	4.19	2861	44.5
S04_30_2	30	0.4	0.49	15.35	24.92	4.22	2815	43.5
S04_30_3	30	0.4	0.48	15.34	24.92	4.22	2824	43.6
S04_45_1	45	0.4	0.50	15.42	24.97	4.21	2777	42.8
S04_45_2	45	0.4	0.52	15.59	25.01	4.20	2861	43.7
S04_45_3	45	0.4	0.50	15.38	24.91	4.19	2713	42.1
I04_0_1	0	0.4	0.97	15.20	24.81	4.22	3355	52.3
I04_0_2	0	0.4	1.00	15.26	24.82	4.24	3311	51.2
I04_0_3	0	0.4	0.98	15.27	24.84	4.20	3327	51.9
I04_30_1	30	0.4	0.99	15.26	24.97	4.12	3274	52.1
I04_30_2	30	0.4	1.00	15.28	24.98	4.18	3262	51.1
I04_30_3	30	0.4	0.99	15.27	24.96	4.16	3260	51.3
I04_45_1	45	0.4	1.01	15.38	25.00	4.18	3206	49.9
I04_45_2	45	0.4	1.02	15.29	24.98	4.12	3182	50.5
I04_45_3	45	0.4	1.03	15.26	24.99	4.16	3174	50.0
B04_0_1	0	0.4	3.00	15.09	24.93	4.32	3330	51.1
B04_0_2	0	0.4	3.00	15.21	24.90	4.26	3307	51.0
B04_0_3	0	0.4	3.00	15.12	24.92	4.30	3294	50.7
B04_30_1	30	0.4	3.00	15.16	25.10	4.39	2986	44.9
B04_30_2	30	0.4	3.00	15.20	25.60	4.30	2706	41.4
B04_30_3	30	0.4	3.00	15.16	25.09	4.32	3099	47.3
B04_45_1	45	0.4	3.00	15.18	25.07	4.20	3179	49.9
B04_45_2	45	0.4	3.00	15.15	25.12	4.22	3230	50.5
B04_45_3	45	0.4	3.00	15.19	25.12	4.26	3163	48.9

Table 3. Summary of the experimental results generated by testing the U-notched specimens under tension (Figs 3a, 3b, and 3c).

Code	θ_P	t_s	α	r_n	w_n	w_g	t	F_f	σ_f
	[°]	*[mm]*	*[Deg]*	*[mm]*	*[mm]*	*[mm]*	*[mm]*	*[N]*	*[MPa]*
OR0_0_1	0	0.4	135	0.46	15.50	25.10	4.21	3302	50.6
OR0_0_2	0	0.4	135	0.48	15.44	25.02	4.18	3329	51.6
OR0_0_3	0	0.4	135	0.52	15.46	25.13	4.18	3325	51.4
OR0_30_1	30	0.4	135	0.44	15.67	25.21	4.18	3057	46.7
OR0_30_2	30	0.4	135	0.44	15.61	25.22	4.20	3108	47.4
OR0_30_3	30	0.4	135	0.48	15.30	25.10	4.19	3068	47.9
OR0_45_1	45	0.4	135	0.56	15.44	24.98	4.20	2858	44.1
OR0_45_2	45	0.4	135	0.57	15.39	25.03	4.17	3015	47.0
OR0_45_3	45	0.4	135	0.48	15.46	25.04	4.18	2960	45.8
OR1_0_1	0	0.4	135	1.01	15.32	24.92	4.24	2670	41.1
OR1_0_2	0	0.4	135	1.05	15.34	25.40	4.21	3031	46.9
OR1_0_3	0	0.4	135	1.01	15.54	25.14	4.21	2669	40.8
OR1_30_1	30	0.4	135	1.04	15.40	25.09	4.20	2543	39.3
OR1_30_2	30	0.4	135	1.00	15.40	25.10	4.22	2889	44.5
OR1_30_3	30	0.4	135	1.04	15.34	25.06	4.22	2472	38.2
OR1_45_1	45	0.4	135	1.04	15.44	25.12	4.20	2939	45.3
OR1_45_2	45	0.4	135	1.01	15.28	25.06	4.21	2893	45.0
OR1_45_3	45	0.4	135	1.05	15.48	25.28	4.19	2825	43.6
OR3_0_1	0	0.4	135	3.01	15.28	25.04	4.13	3195	50.6
OR3_0_2	0	0.4	135	3.02	15.18	24.99	4.11	3297	52.8
OR3_0_3	0	0.4	135	3.03	15.22	25.04	4.11	3216	51.4
OR3_30_1	30	0.4	135	3.00	15.38	25.15	4.12	3142	49.6
OR3_30_2	30	0.4	135	3.05	15.38	25.26	4.09	3195	50.8
OR3_30_3	30	0.4	135	2.98	15.36	25.14	4.11	3069	48.6
OR3_45_1	45	0.4	135	3.02	15.47	25.30	4.07	2826	44.9
OR3_45_2	45	0.4	135	2.99	15.25	25.10	4.10	2872	45.9
OR3_45_3	45	0.4	135	3.04	15.44	25.18	4.08	2997	47.6

Table 4. Summary of the experimental results generated by testing under tension the specimens containing open notches (Figs 3d, 3e, and 3f).

Code	θ_P	t_s	α	r_n	w_n	w_g	t	F_f	σ_f
	[°]	*[mm]*	*[Deg]*	*[mm]*	*[mm]*	*[mm]*	*[mm]*	*[N]*	*[MPa]*
BR0_0_1	0	0.4	30	0.05	15.44	24.95	4.30	1009	73.8
BR0_0_2	0	0.4	30	0.04	15.46	24.96	4.23	1049	77.8
BR0_0_3	0	0.4	30	0.05	15.44	25.02	4.24	1063	78.9
BR0_30_1	30	0.4	30	0.06	15.48	25.20	4.23	810	60.0
BR0_30_2	30	0.4	30	0.05	15.42	25.27	4.26	-	-
BR0_30_3	30	0.4	30	0.05	15.50	25.12	4.26	847	62.1
BR0_45_1	45	0.4	30	0.04	14.78	25.14	4.28	879	70.5
BR0_45_2	45	0.4	30	0.04	14.80	25.06	4.26	884	71.0
BR0_45_3	45	0.4	30	0.06	14.91	25.13	4.29	862	67.8
BR1_0_1	0	0.4	0	1.02	14.98	25.08	4.28	1096	85.6
BR1_0_2	0	0.4	0	1.01	14.98	25.03	4.28	1050	82.0
BR1_0_3	0	0.4	0	0.98	14.96	25.00	4.28	1054	82.5
BR1_30_1	30	0.4	0	0.97	14.97	25.04	4.28	813	63.6
BR1_30_2	30	0.4	0	0.99	14.96	25.06	4.28	865	67.7
BR1_30_3	30	0.4	0	1.00	14.96	24.92	4.32	803	62.3
BR1_45_1	45	0.4	0	1.01	15.06	24.68	4.28	895	69.1
BR1_45_2	45	0.4	0	1.01	15.04	24.89	4.31	926	71.3
BR1_45_3	45	0.4	0	0.97	15.04	24.82	4.32	850	65.2
R3_0_1	0	0.4	0	3.11	14.98	24.88	4.23	1144	90.4
R3_0_2	0	0.4	0	3.03	15.07	24.90	4.26	1131	87.7
R3_0_3	0	0.4	0	2.91	15.07	24.90	4.20	1134	89.2
BR3_30_1	30	0.4	0	2.95	15.08	24.89	4.18	875	69.0
BR3_30_2	30	0.4	0	2.98	15.08	24.90	4.16	873	69.2
BR3_30_3	30	0.4	0	3.07	15.09	24.88	4.26	874	67.6
BR3_45_1	45	0.4	0	3.09	15.09	24.92	4.22	923	72.0
BR3_45_2	45	0.4	0	3.01	15.09	24.94	4.20	930	72.9
BR3_45_3	45	0.4	0	2.94	15.08	25.02	4.17	-	-

Table 5. Summary of the experimental results generated by testing the U-notched specimens under three-point bending (Figs 3g, 3h, and 3i).

Code	θ_P	t_s	α	r_n	w_n	w_g	t	F_f	σ_f
	[°]	*[mm]*	*[Deg]*	*[mm]*	*[mm]*	*[mm]*	*[mm]*	*[N]*	*[MPa]*
OBR0_0_1	0	0.4	135	0.35	14.92	25.09	4.17	990	96.0
OBR0_0_2	0	0.4	135	0.33	14.98	24.92	4.19	1015	97.1
OBR0_0_3	0	0.4	135	0.34	14.98	25.01	4.16	996	96.0
OBR0_30_1	30	0.4	135	0.35	15.00	25.06	4.18	701	67.1
OBR0_30_2	30	0.4	135	0.39	15.01	25.18	4.14	786	75.8
OBR0_30_3	30	0.4	135	0.34	15.00	25.02	4.16	776	74.6
OBR0_45_1	45	0.4	135	0.37	15.14	24.93	4.16	660	62.3
OBR0_45_2	45	0.4	135	0.39	15.12	24.94	4.14	640	60.9
OBR0_45_3	45	0.4	135	0.31	15.01	24.97	4.18	647	61.9
OBR1_0_1	0	0.4	135	0.99	14.99	24.72	4.19	919	87.8
OBR1_0_2	0	0.4	135	1.02	15.08	24.72	4.18	939	88.9
OBR1_0_3	0	0.4	135	1.01	15.16	24.88	4.16	924	86.9
OBR1_30_1	30	0.4	135	0.98	15.14	24.82	4.16	696	65.7
OBR1_30_2	30	0.4	135	1.01	15.28	24.88	4.16	690	64.0
OBR1_30_3	30	0.4	135	1.03	15.18	24.88	4.16	693	65.0
OBR1_45_1	45	0.4	135	0.99	15.06	24.76	4.20	649	61.3
OBR1_45_2	45	0.4	135	0.99	15.12	24.78	4.22	636	59.3
OBR1_45_3	45	0.4	135	1.02	15.03	24.78	4.24	641	60.3
OBR3_0_1	0	0.4	135	3.01	14.88	24.90	4.10	887	87.9
OBR3_0_2	0	0.4	135	3.02	14.98	24.90	4.09	902	88.4
OBR3_0_3	0	0.4	135	2.99	14.98	24.96	4.10	907	88.7
OBR3_30_1	30	0.4	135	2.99	15.03	24.99	4.07	773	75.6
OBR3_30_2	30	0.4	135	3.00	15.04	25.00	4.11	692	67.0
OBR3_30_3	30	0.4	135	3.01	15.02	25.01	4.09	701	68.4
OBR3_45_1	45	0.4	135	3.02	15.02	25.06	4.11	753	73.1
OBR3_45_2	45	0.4	135	2.98	15.02	24.90	4.08	744	72.8
OBR3_45_3	45	0.4	135	2.99	15.04	24.94	4.08	734	71.6

Table 6. Summary of the experimental results generated by testing under three-point bending the specimens containing open notches (Figs 3k, 3l, and 3m).

Code	θ_P	t_s	B	W	a	P_Q	K_c
	[°]	*[mm]*	*[mm]*	*[mm]*	*[mm]*	*[N]*	*[MPa·m$^{1/2}$]*
CT_0_1	0	0.4	20.02	40.05	20.11	1890	4.6
CT_0_2	0	0.4	20.12	39.98	20.01	1948	4.7
CT_0_3	0	0.4	20.08	40.03	20.07	1871	4.5
CT_30_1	30	0.4	20.11	40.02	19.98	1749	4.2
CT_30_2	30	0.4	20.10	40.11	20.02	1575	3.8
CT_30_3	30	0.4	20.12	39.96	20.02	1610	3.9
CT_45_1	45	0.4	20.07	40.02	20.03	1746	4.2
CT_45_2	45	0.4	20.08	39.98	20.11	1728	4.2
CT_45_3	45	0.4	20.08	39.97	20.04	1744	4.2
CT30_45_1	0	0.4	30.09	60.04	30.12	2828	3.7
CT30_45_2	0	0.4	30.11	60.03	30.08	2837	3.7
CT30_45_3	0	0.4	30.03	60.03	29.99	2832	3.7

Table 7. Summary of the experimental results generated by testing the C(T) specimens (Figs 2c and 2d).

Figures

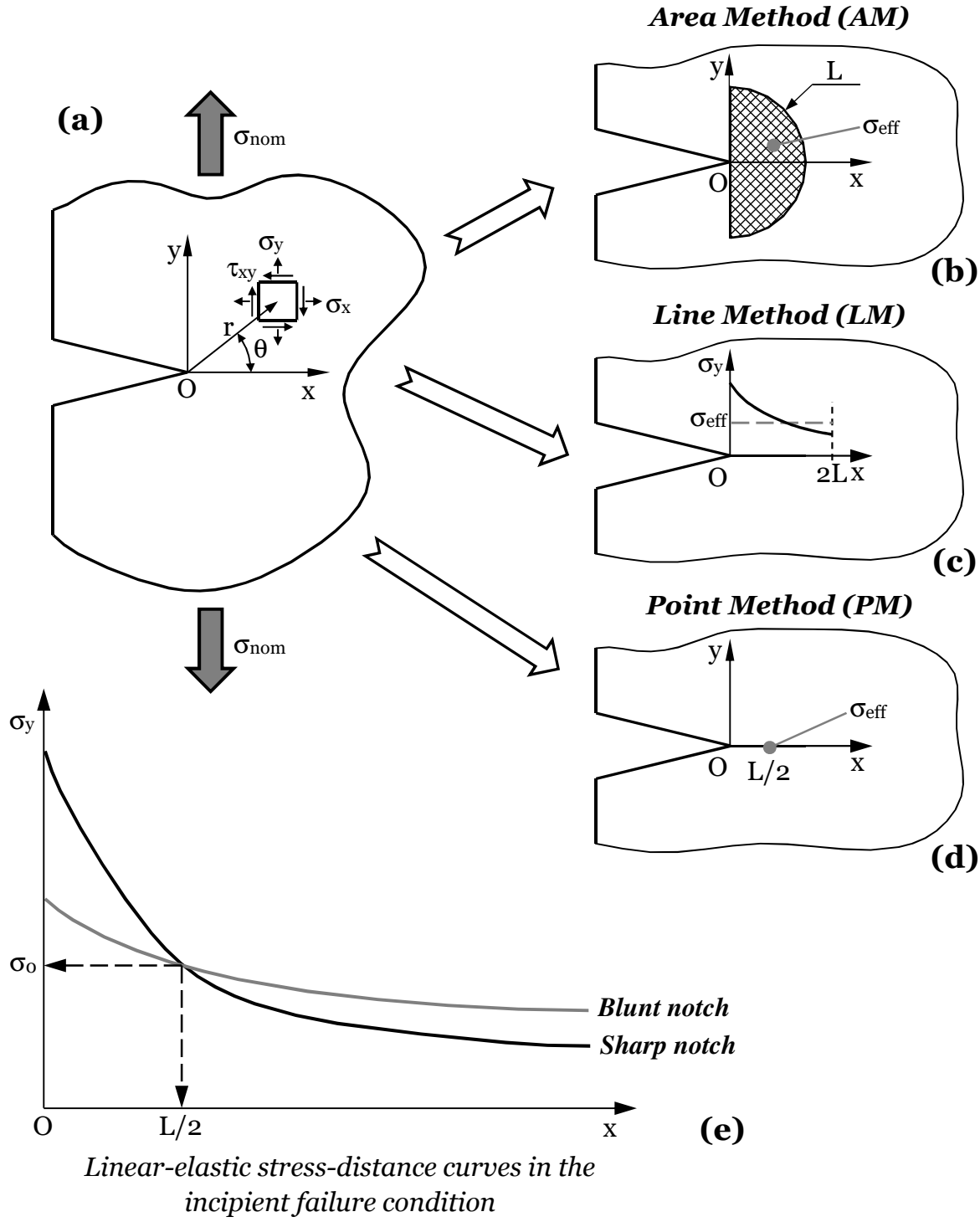

Linear-elastic stress-distance curves in the incipient failure condition

Figure 1. Local system of coordinates (a); effective stress calculated according to the AM (b), to the LM (c) and to the PM (d); inherent strength σ_0 and critical distance L determined from experimental results generated by testing notches of different sharpness (d).

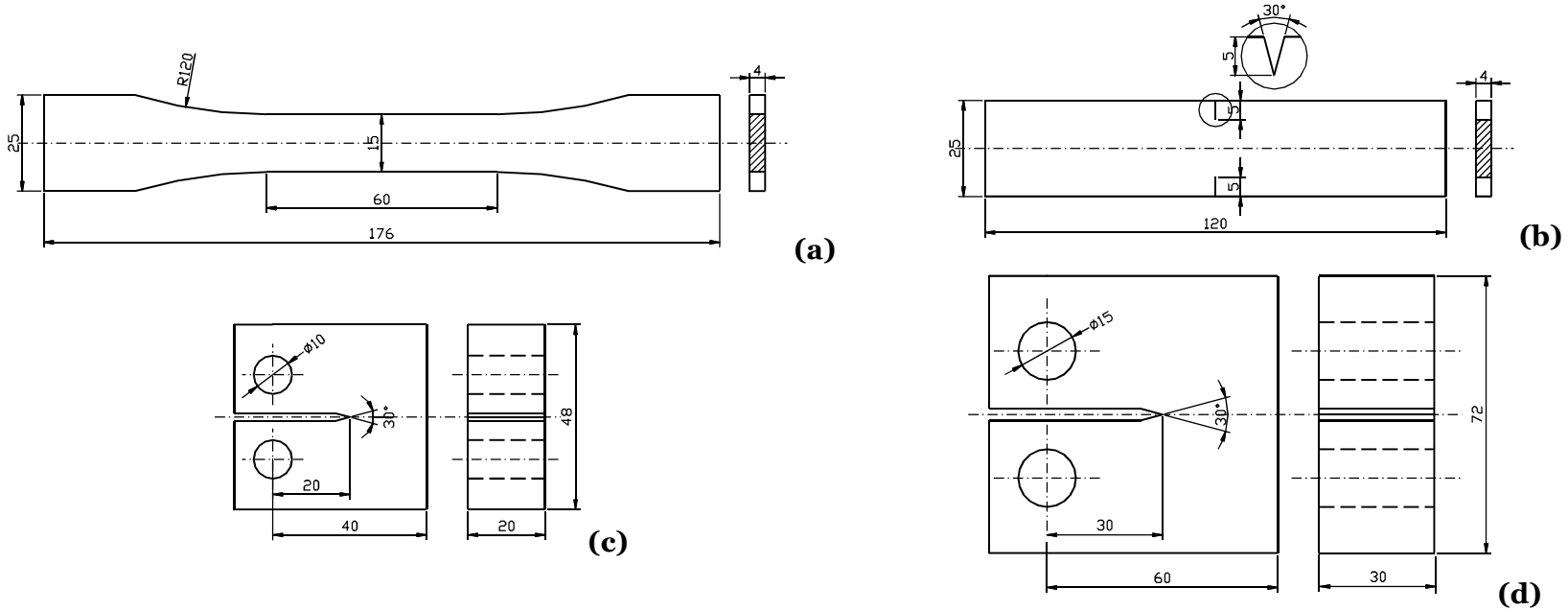

Figure 2. Geometries of the plain specimens (a), the samples containing crack-like notches (b) as well as of the C(T) specimens (c, d) – Nominal dimensions in millimieters.

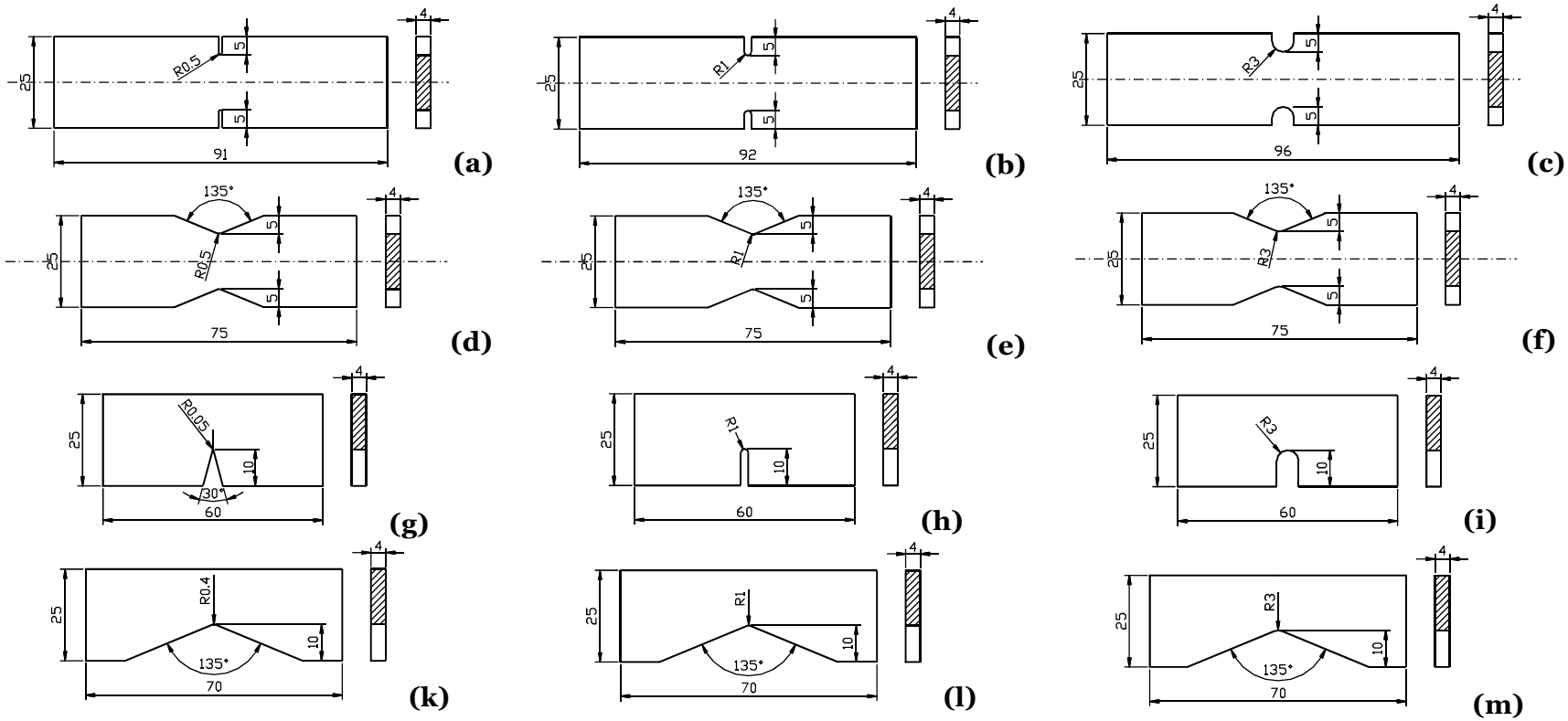

Figure 3. Geometries of the notched specimens – Nominal dimensions in millimetres.

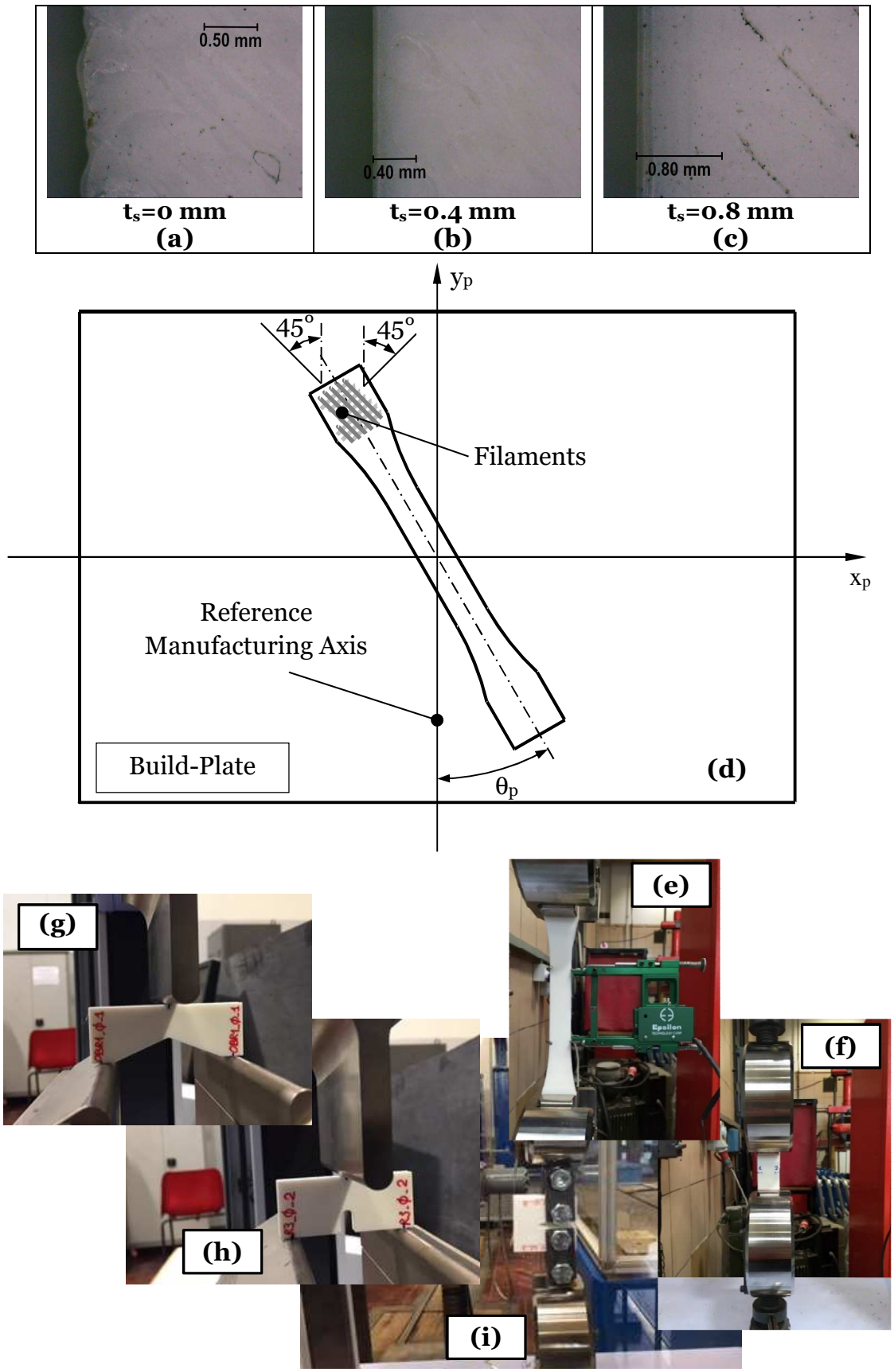

Figure 4. Specimens manufactured by setting the shell thickness, t_s, equal to 0 mm (a), to 0.4 mm (b) , and 0.8 mm (c); definition of manufacturing angle θ_p and orientation of the deposition filaments (d); examples showing the different testing set-ups that were used to test plain specimens under tension (e), samples with opposite notches under tension (f), rectangular plate with single notch under three-point bending (g, h) and C(T) specimens (i).

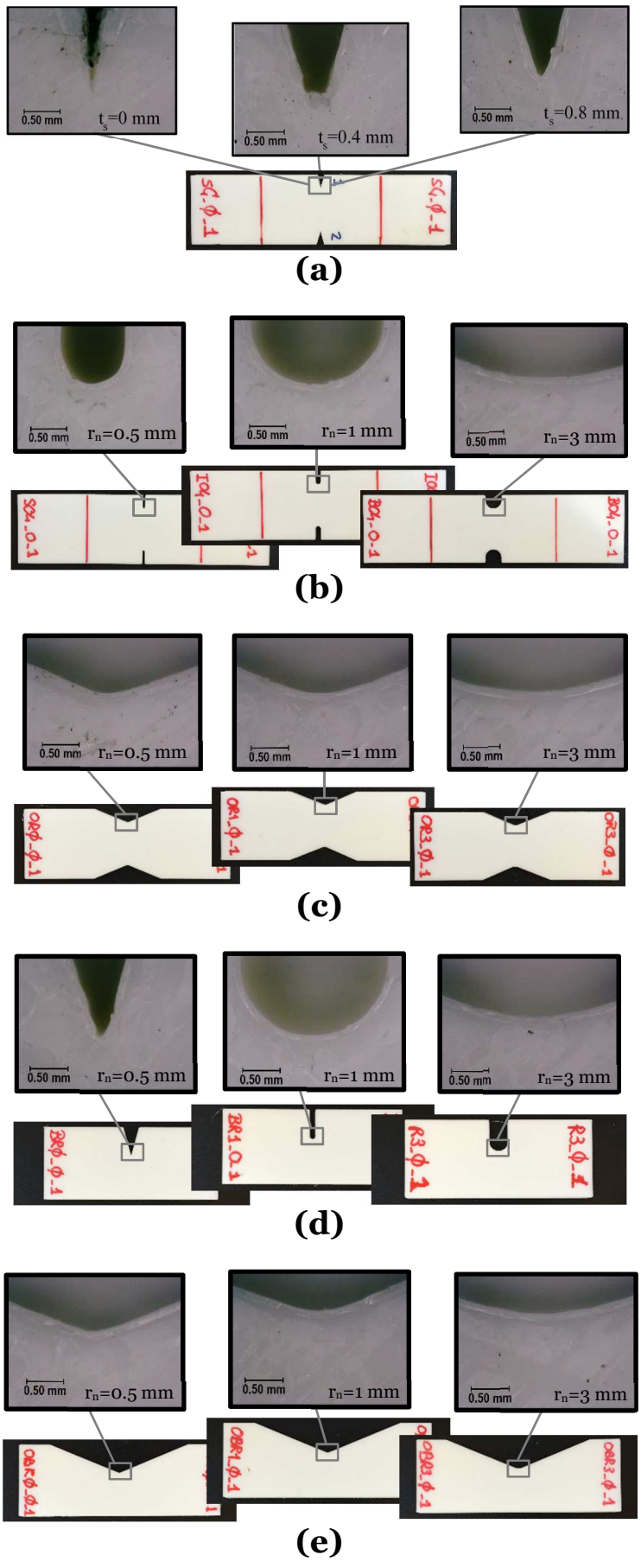

Figure 5. Examples showing some of the notched specimens that were tested under tensile loading (a, b, c) as well as under three-point bending (d, e).

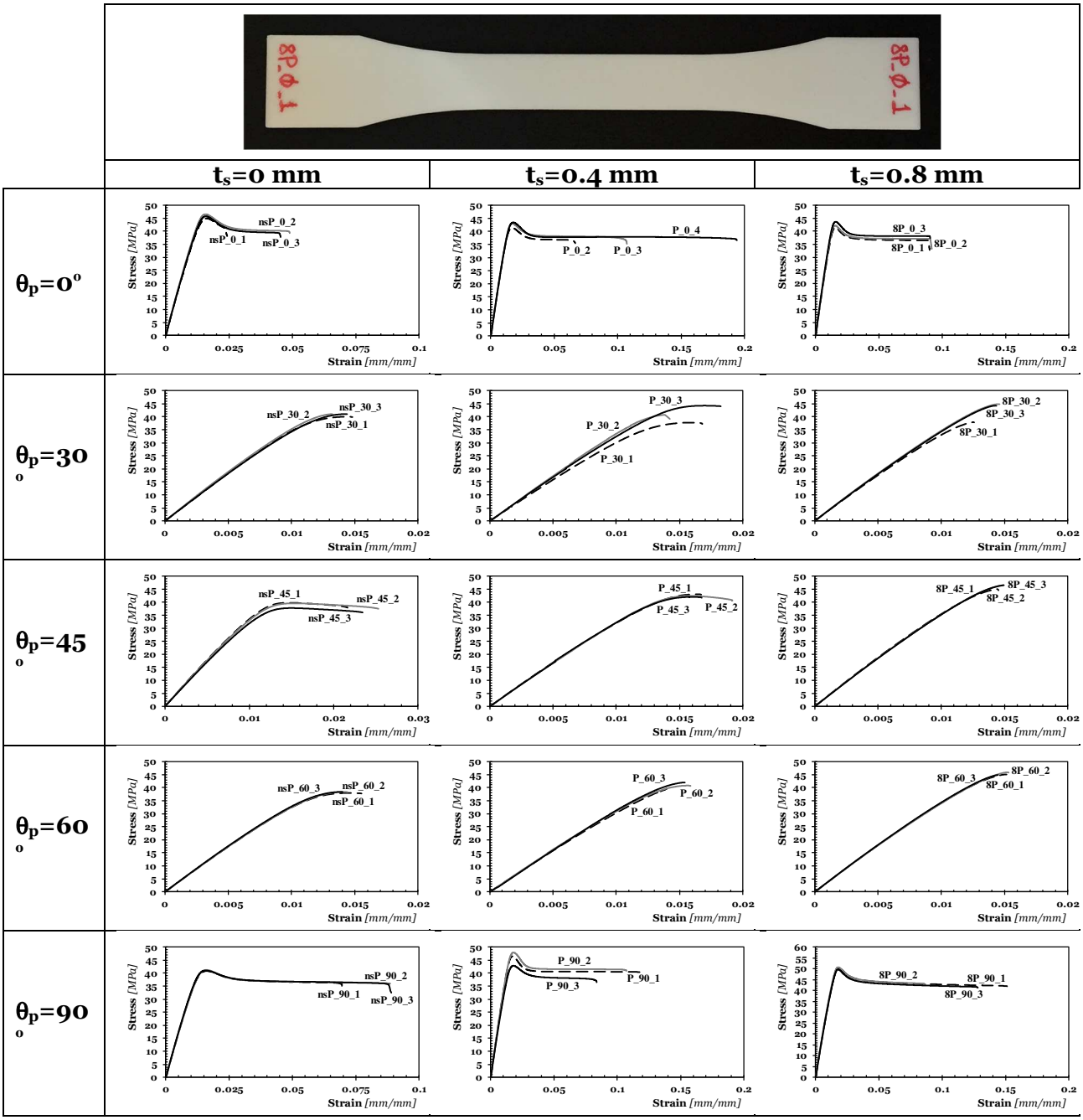

Figure 6. Stress vs. strain curves generated by testing the plain specimens under tensile loading.

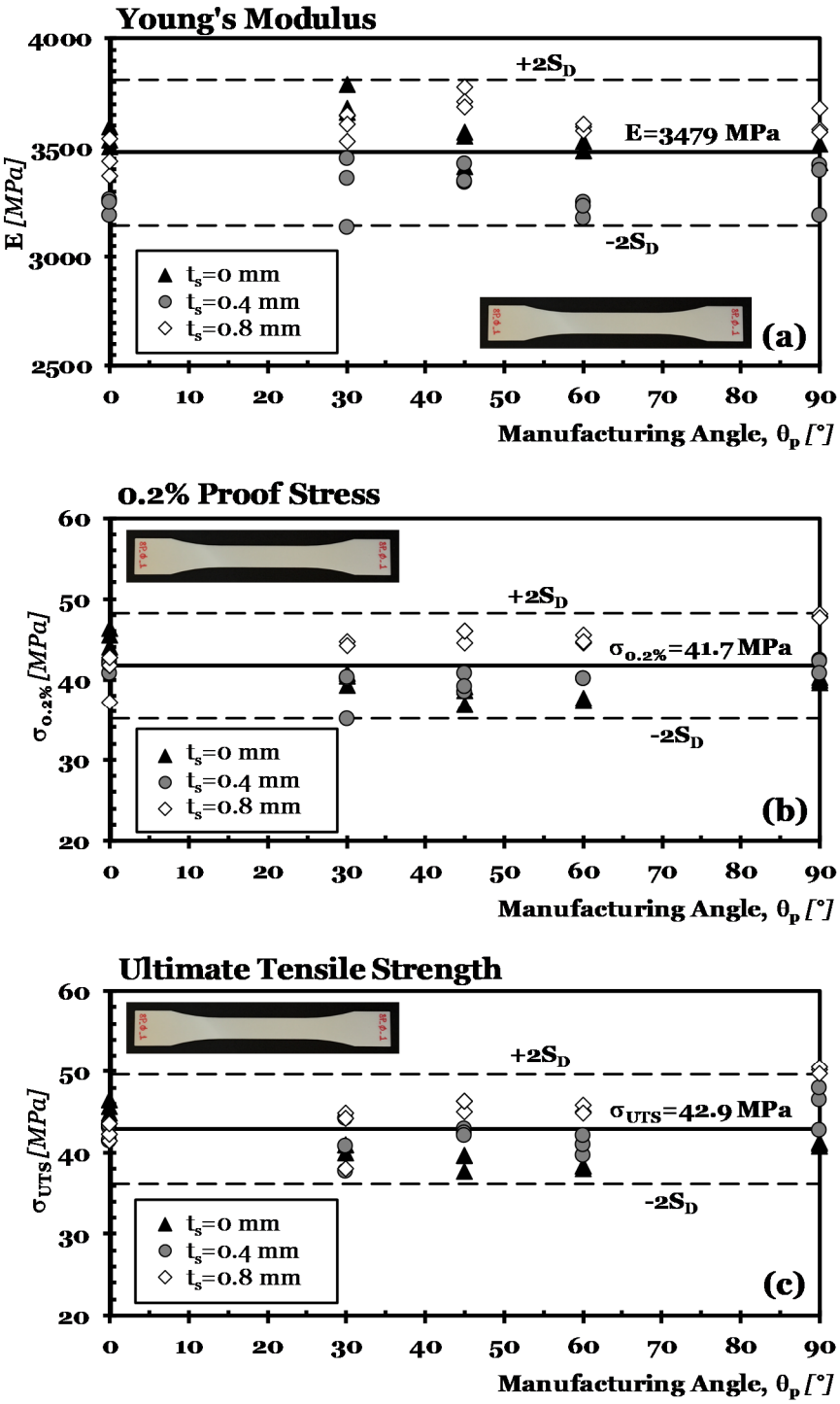

Figure 7. Summary of the mechanical properties determined by testing plain specimens with t_s=0, 0.4, 0.8 mm and θ_p=0°, 30°, 45°, 60°, 90°.

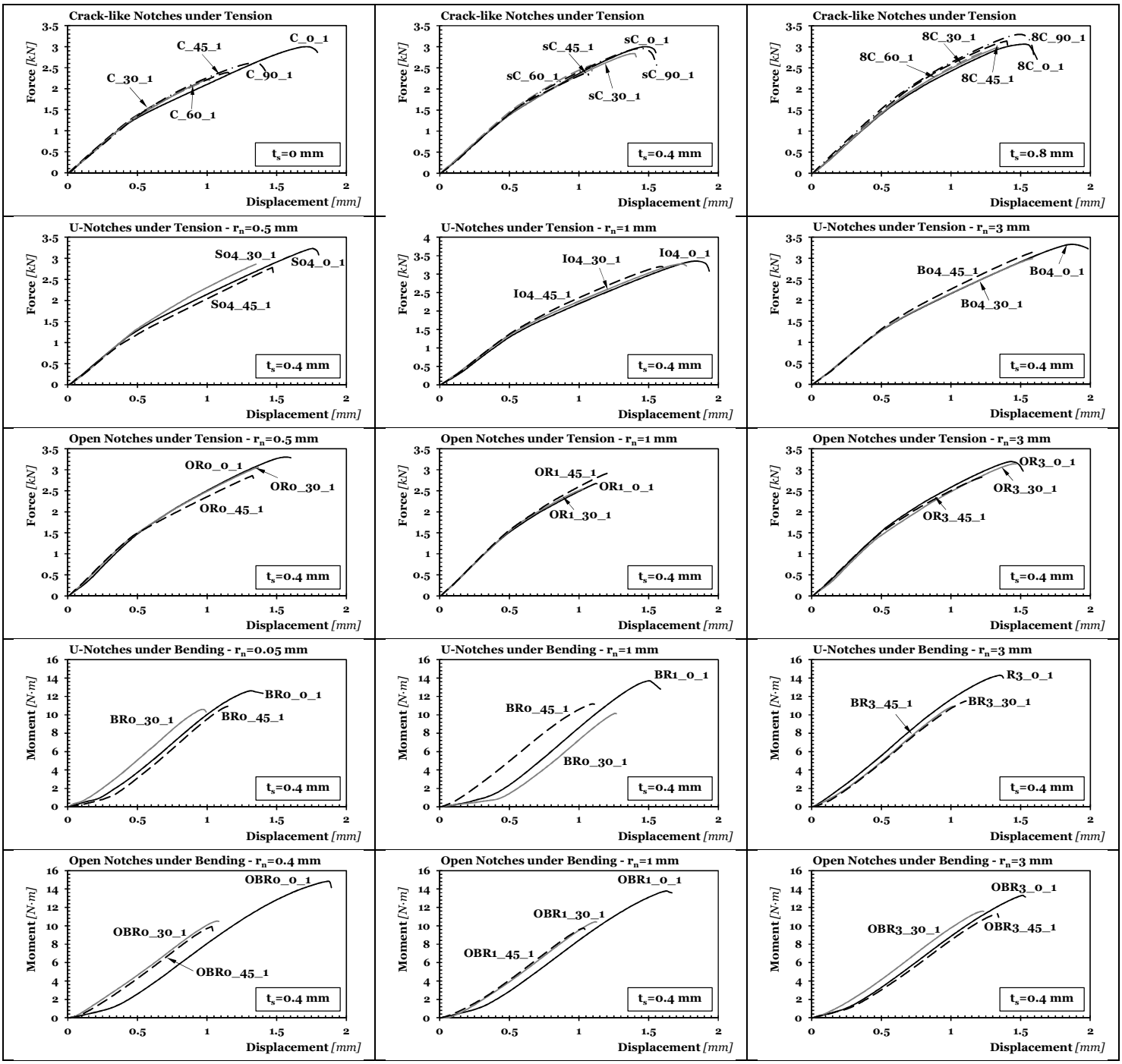

Figure 8. Examples of force/moment vs. displacement curves generated by testing the notched specimens under tensile/bending loading.

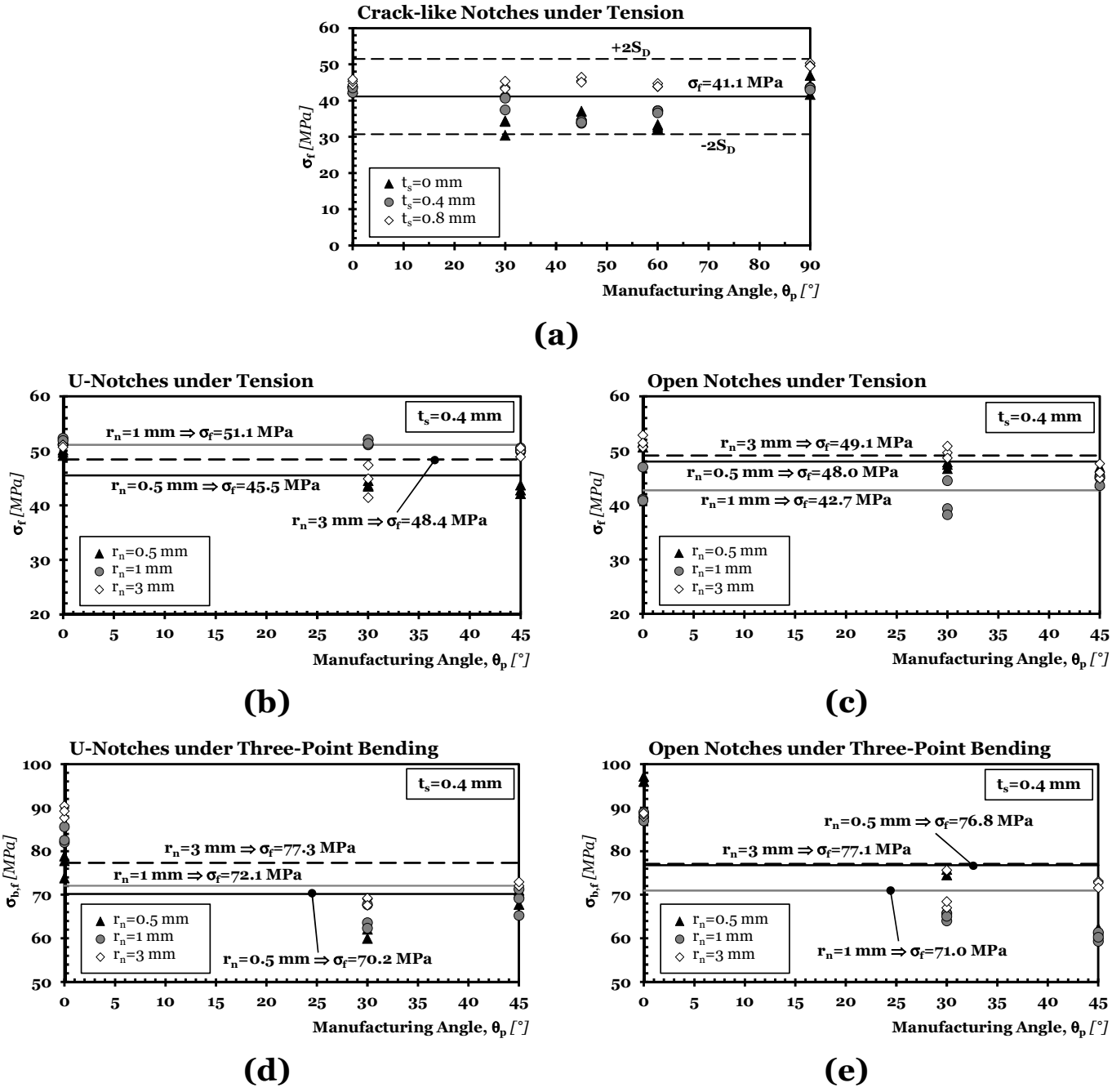

Figure 9. Static Strength of the notched specimens tested under tension as well as under three-point bending.

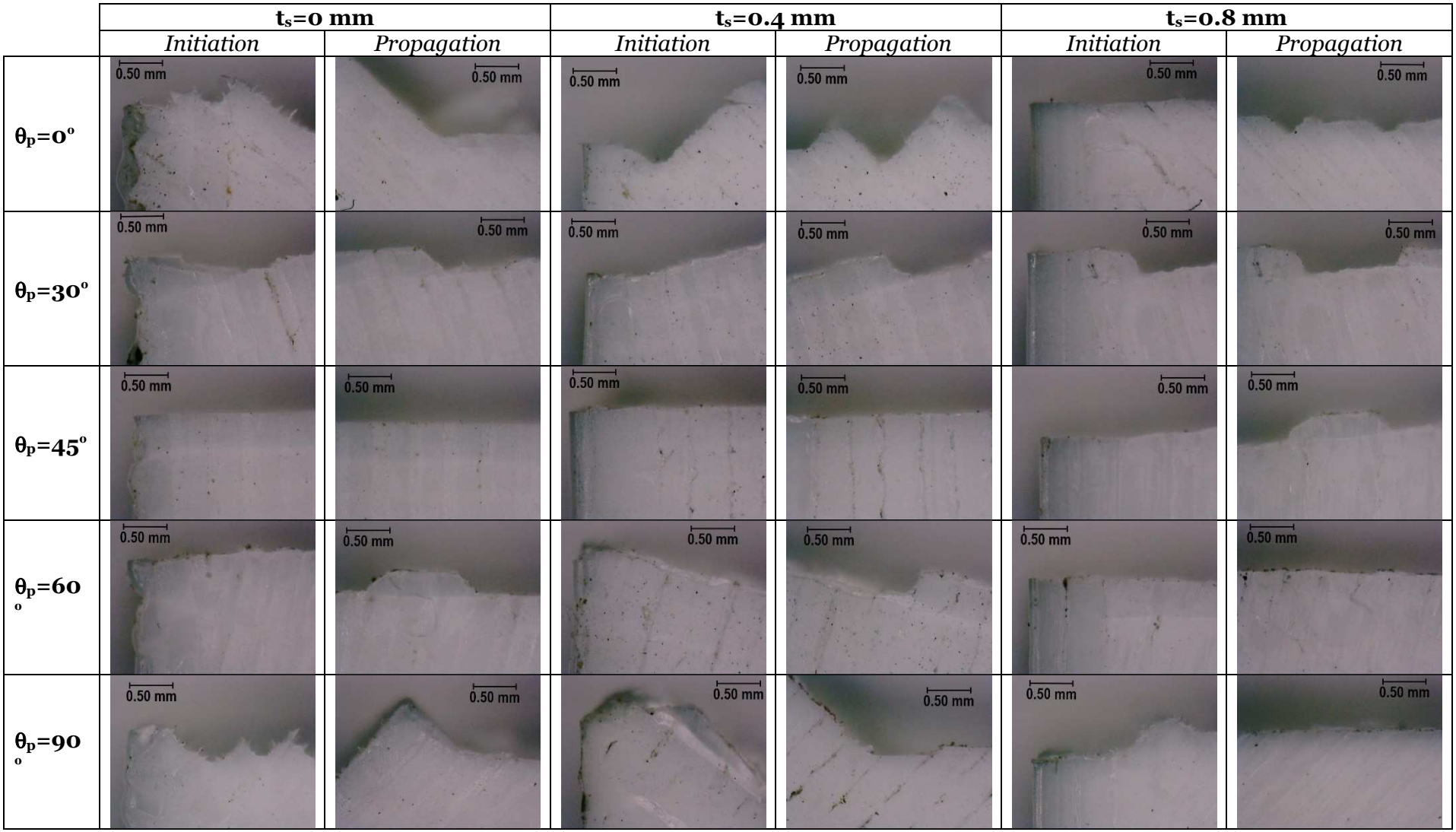

Figure 10. Matrix summarising the cracking behaviour displayed by the plain material (in the pictures showing the crack initiation region the edge of the specimen is on the left hand side).

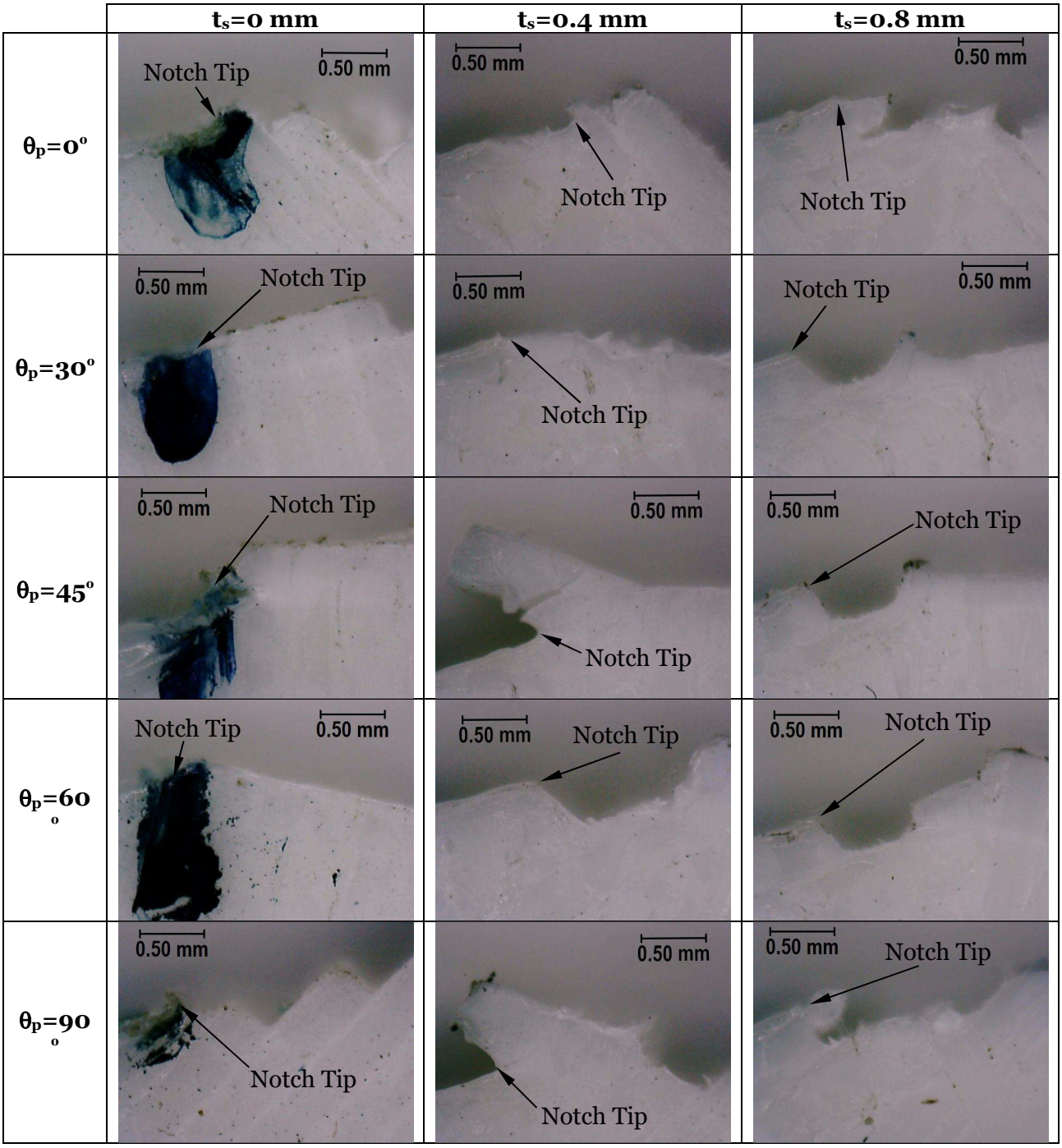

Figure 11. Matrix summarising the crack initiation process observed in the specimens containing crack-like notches (the specimens' longitudinal axis is vertical).

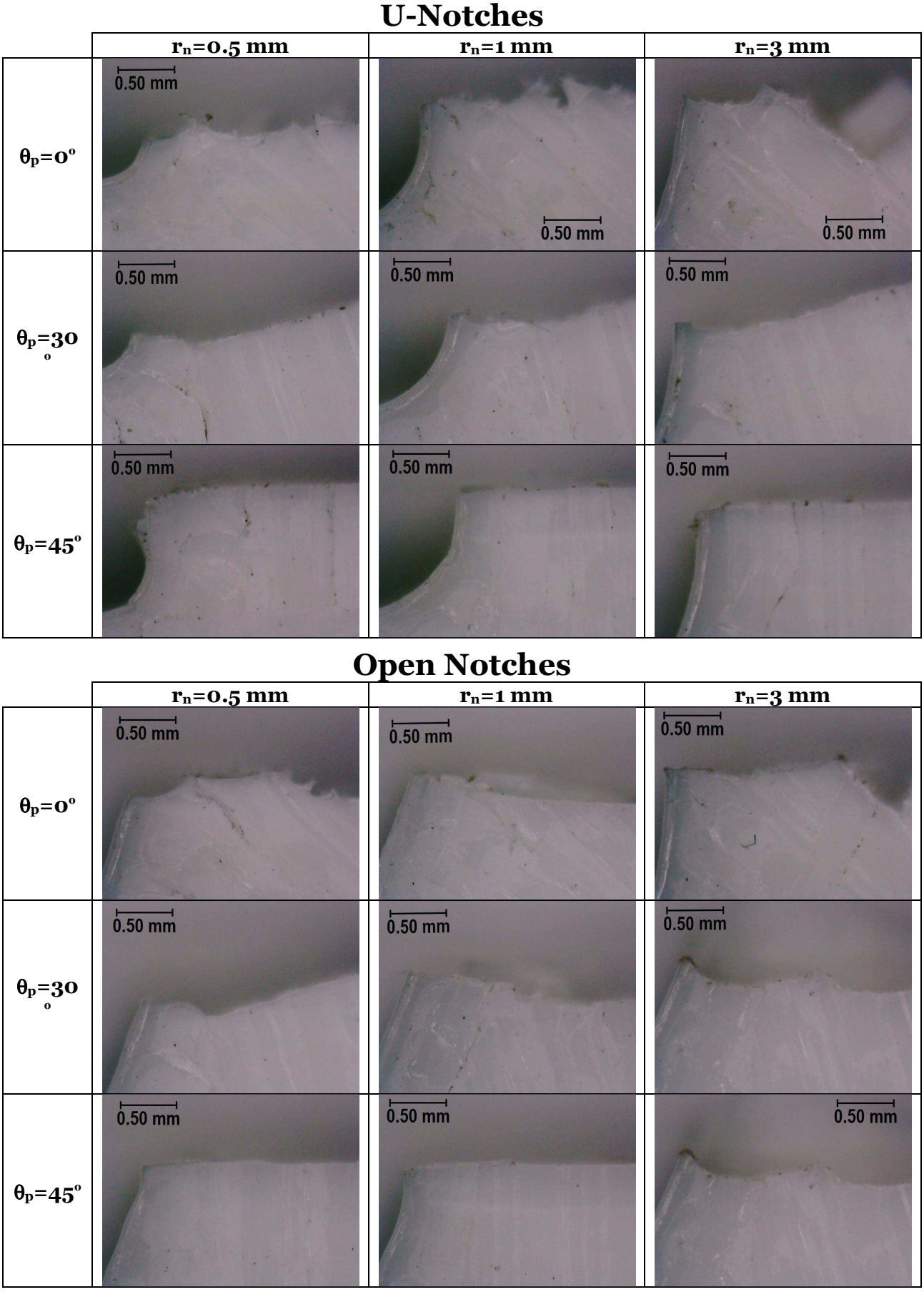

Figure 12. Crack initiation process observed under tensile loading in the specimens containing both U- and open notches (t_s=0.4 mm) - the specimens' longitudinal axis is vertical.

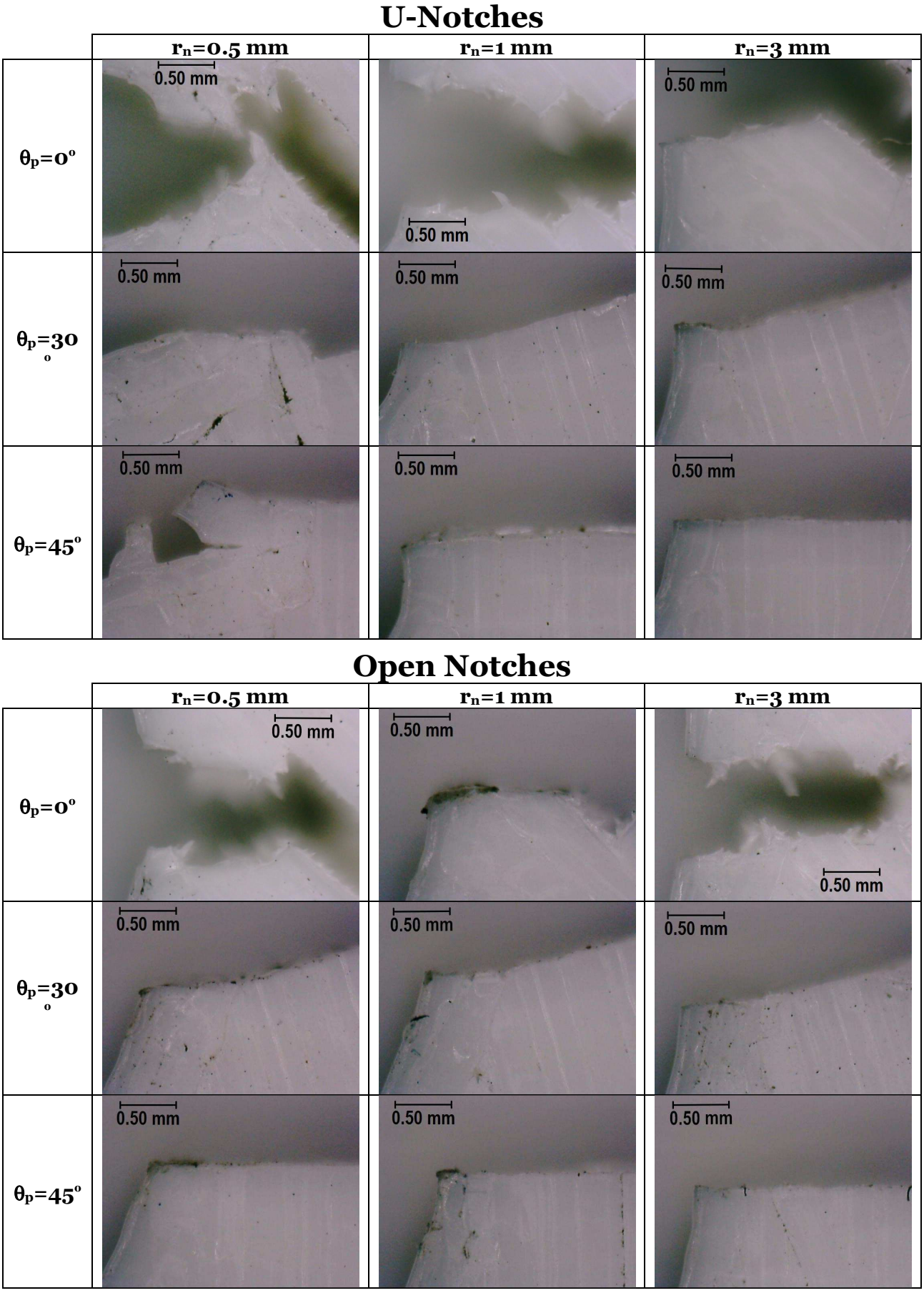

Figure 13. Crack initiation process observed under three-point bending in the specimens containing both U- and open notches (t_s=0.4 mm) - the specimens' longitudinal axis is vertical.

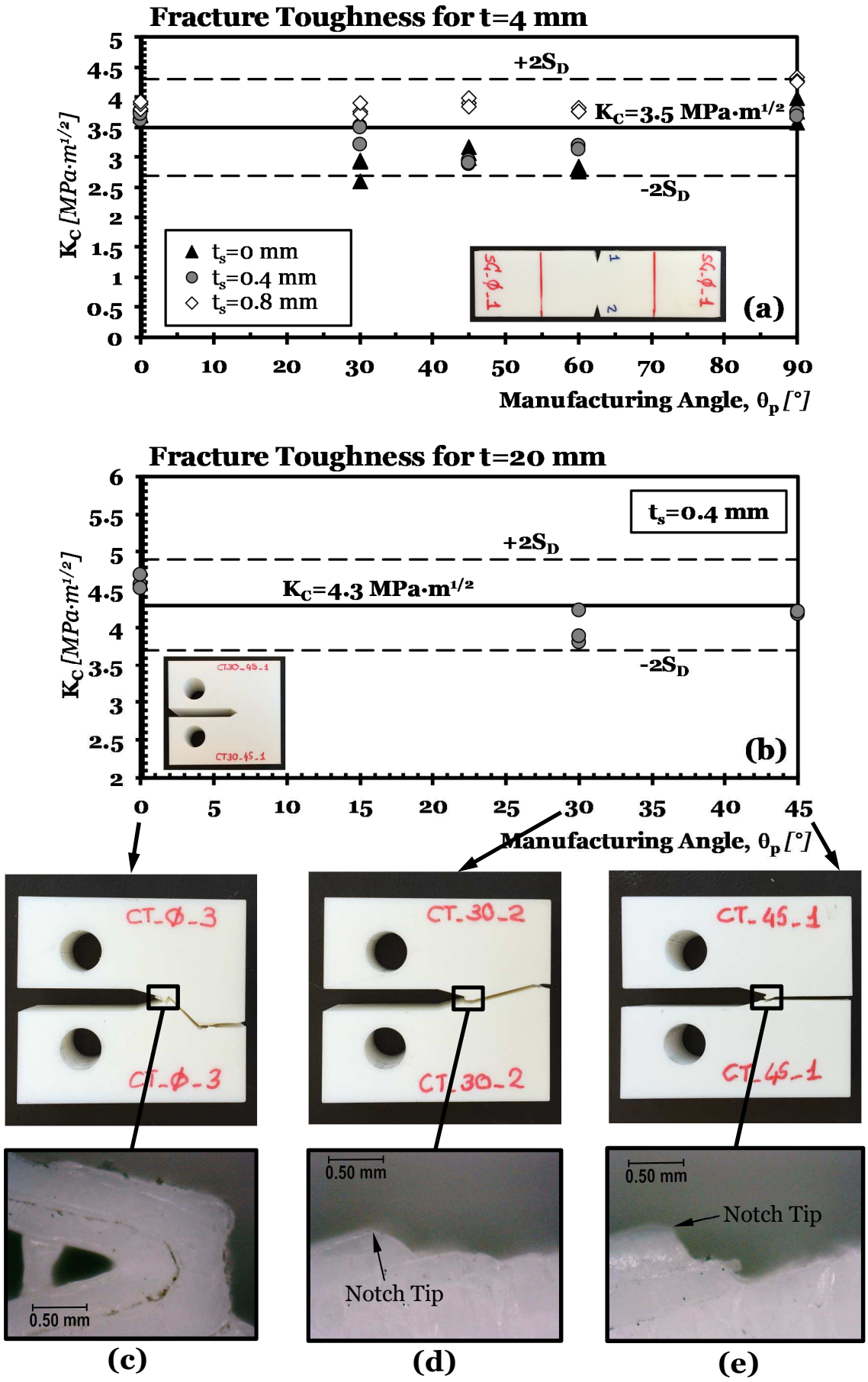

Figure 14. Fracture toughness values for t=4 mm (a) and t=20 mm (b); examples of cracking behaviour displayed by the C(T) specimens with t=20 mm (c, d, e).

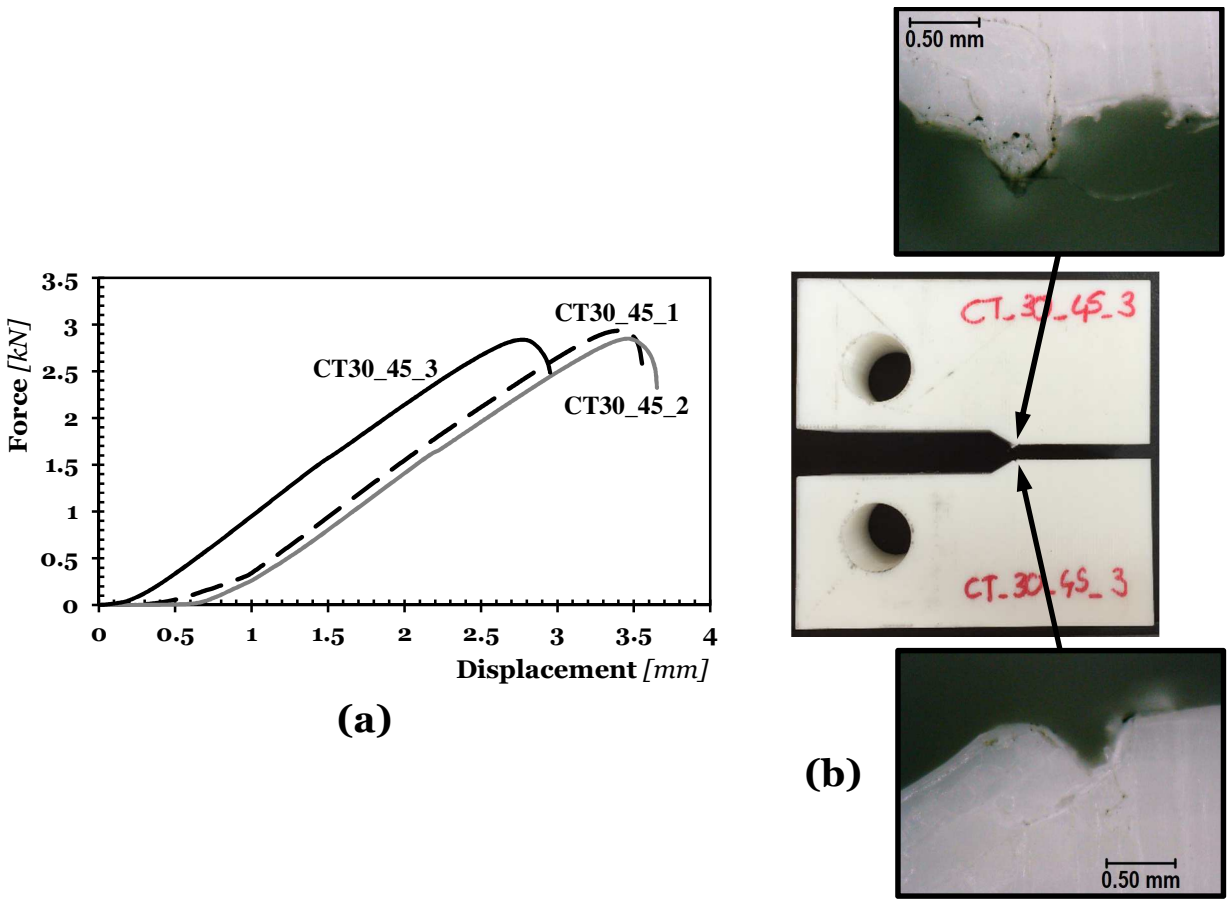

Figure 15. Force vs. displacement curves generated by testing C(T) specimens having thickness equal to 30 mm and manufacturing by setting θ_p equal to 45° and t_s to 0.4 mm (a); Mode I fracture in specimen CT_30_45_3 (b).

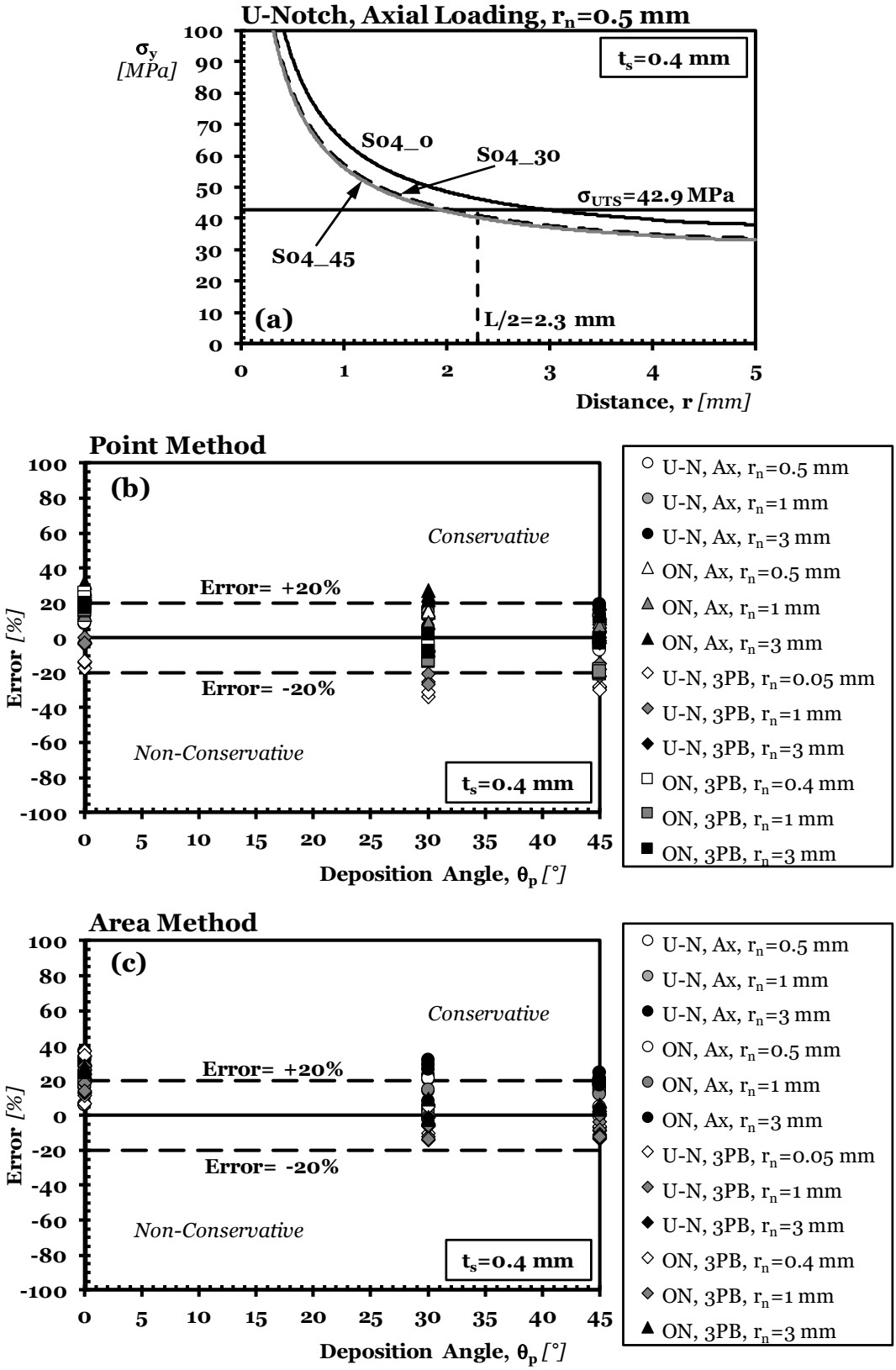

Figure 16. Determination of critical distance L (a); accuracy of the PM (b) and the LM (b) in estimating static strength of notched AM PLA (U-N = U-notch; ON = open notch; Ax = axial loading; 3PB = three-point bending).